iScience

CellPress
OPEN ACCESS

Article

Spastin regulates ER-mitochondrial contact sites and mitochondrial homeostasis

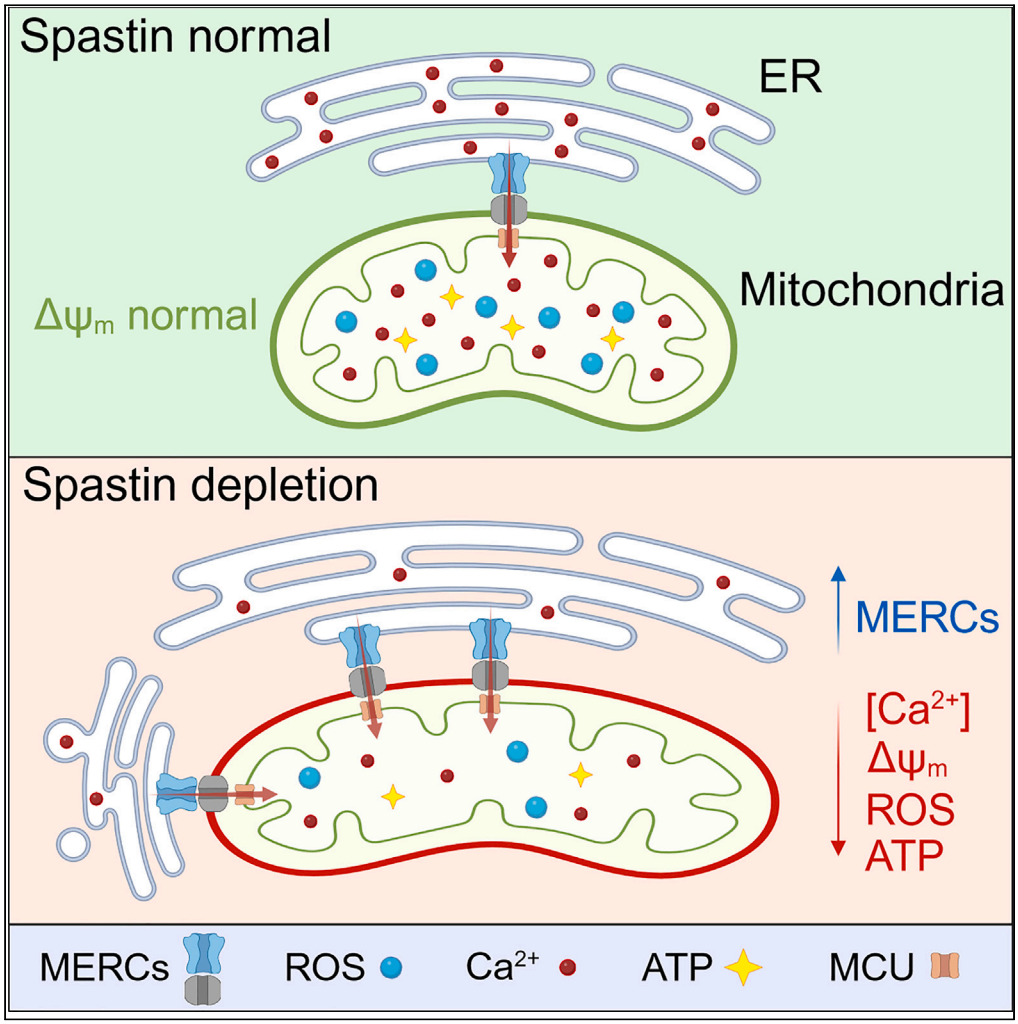

Amelie Raby, Sonia Missiroli, Peggy Sanatine, ..., Paolo Pinton, Ana Buj-Bello, Andrea Burgo

andrea.burgo@univ-evry.fr

Highlights

Spastin localizes in mitochondria-ER contact sites (MERCs)

Spastin expression levels regulate MERCs number

Loss of spastin decreases ER and mitochondrial calcium content

Spastin depletion impairs ΔΨm, ROS levels, and OXPHOS

Raby et al., iScience 27, 110683
September 20, 2024
https://doi.org/10.1016/j.isci.2024.110683

iScience

CellPress
OPEN ACCESS

Article

Spastin regulates ER-mitochondrial contact sites and mitochondrial homeostasis

Amelie Raby,[1,2,6] Sonia Missiroli,[3,6] Peggy Sanatine,[1] Dominique Langui,[4] Julien Pansiot,[5] Nissai Beaude,[1,2] Lucie Vezzana,[1,2] Rachelle Saleh,[5] Martina Marinello,[1,2] Mireille Laforge,[5] Paolo Pinton,[3] Ana Buj-Bello,[1,2] and Andrea Burgo[1,2,7,*]

SUMMARY

Mitochondria-endoplasmic reticulum (ER) contact sites (MERCs) emerged to play critical roles in numerous cellular processes, and their dysregulation has been associated to neurodegenerative disorders. Mutations in the SPG4 gene coding for spastin are among the main causes of hereditary spastic paraplegia (HSP). Spastin binds and severs microtubules, and the long isoform of this protein, namely M1, spans the outer leaflet of ER membrane where it interacts with other ER-HSP proteins. Here, we showed that overexpressed M1 spastin localizes in ER-mitochondria intersections and that endogenous spastin accumulates in MERCs. We demonstrated in different cellular models that downregulation of spastin enhances the number of MERCs, alters mitochondrial morphology, and impairs ER and mitochondrial calcium homeostasis. These effects are associated with reduced mitochondrial membrane potential, oxygen species levels, and oxidative metabolism. These findings extend our knowledge on the role of spastin in the ER and suggest MERCs deregulation as potential causes of SPG4-HSP disease.

INTRODUCTION

Spastin, encoded by the *SPG4* gene (*SPAST* in humans), is an ATP-powered severing enzyme containing a C-terminal ATPase associated with diverse cellular activities (AAAs) domain that cut microtubules (MTs) into smaller fragments.[1,2] Mutations in *SPAST* account for 40% of autosomal dominant and 20% of sporadic cases of hereditary spastic paraplegia (HSP).[3] Over 300 different mutations have been identified in *SPAST*, and although still controversial,[4] a loss of function (i.e., haploinsufficiency) is likely the main pathological mechanism involved in the disease. This neurological disorder is caused by degeneration of the long axons of descending corticospinal tract and ascending sensory fibers, leading to progressive spasticity and weakness of lower limbs in SPAST-HSP patients.[5] *SPG4* can be translated mainly in two different isoforms of spastin,[6] the full-length M1 and the shorter M87 (M85 in rodent), the latter lacking the first 87 aa (85 aa in rodent) of the N-terminal part of M1. This N-terminal sequence confers M1's unique ability to insert the protein into the outer leaflet of the ER membrane.[7] At the ER membrane, M1 interacts with several ER-shaping proteins also involved in HSPs such as atlastin-1 (SPG3A),[8,9] REEP1 (SPG31),[7] and reticulons such as RTN1[10] and RTN2 (SPG12).[11] These proteins can modulate the ER morphology and functions by partially spanning the ER membrane and inducing or stabilizing the curvature of ER tubules via hydrophobic wedges.[7,12,13] Spastin plays key roles in many cellular processes that involve MT dynamics such as axonal transport, endosomal trafficking, and cytokinesis.[14] Based on its intracellular localization, MT-severing activity, and interaction with ER-shaping proteins, the M1 isoform was proposed to regulate ER morphology and functions. However, to date experimental evidence showing ER defects in pathogenesis of SPG4-related HSP are lacking.[15] In fact, most of the information on the role of ER role of spastin come from studies where wild-type (WT) or mutated form of M1 spastin was overexpressed, which does not mimic the haploinsufficiency mechanism of the disease. In these studies, the alterations observed in ER morphology are likely due to excessive MTs severing or formation of MTs-ER decorated bundles triggered by enzymatically active or inactive spastin, respectively.[8,16] Only recently the downregulation of spastin expression has been associated with altered ER shape, such as an increase in ER thickness[17] or flattened ER[18] in a SPG4-KO cell model and skeletal muscle fibers of Spg4 mutant fish embryos, respectively. Moreover, Drosophila carrying a dominant-negative mutant of spastin leads preferentially to the formation of ER sheets over ER tubules.[19]

[1]Genethon, 91000 Evry, France
[2]Université Paris-Saclay, University Evry, Inserm, Genethon, Integrare Research Unit UMR_S951, 91000 Evry, France
[3]Department of Medical Sciences, Section of Experimental Medicine, University of Ferrara, and Technopole of Ferrara, Laboratory for Advanced Therapies (LTTA), 44121 Ferrara, Italy
[4]Sorbonne Université, Institut du Cerveau - Paris Brain Institute - ICM, Inserm U1127, CNRS, APHP, Hôpital de la Pitié Salpêtrière, Paris, France
[5]Université Paris Cité, NeuroDiderot, Inserm, 75019 Paris, France
[6]These authors contributed equally
[7]Lead contact
*Correspondence: andrea.burgo@univ-evry.fr
https://doi.org/10.1016/j.isci.2024.110683

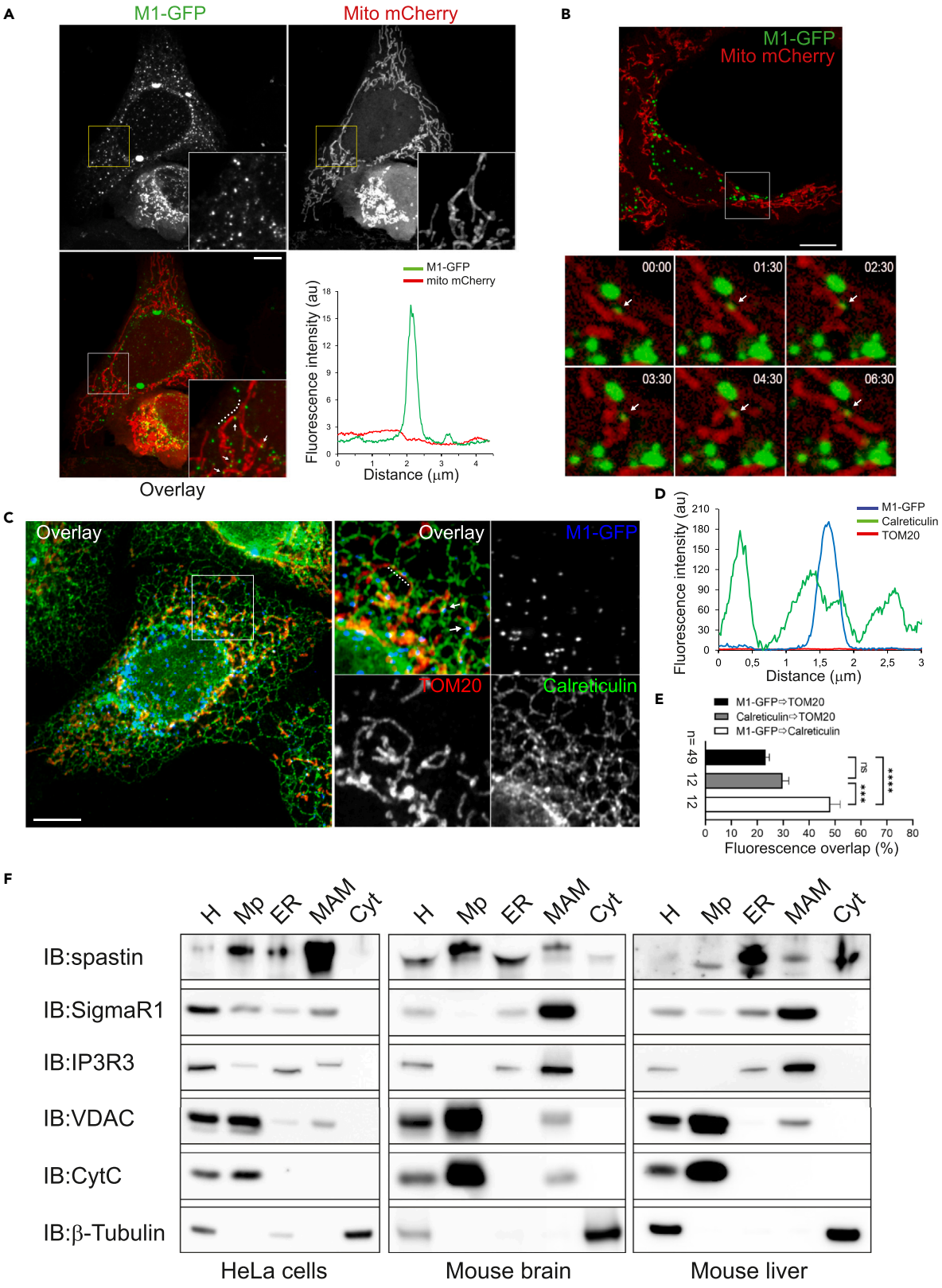
A
M1-GFP
Mito mCherry
Overlay
M1-GFP
mito mCherry
Fluorescence intensity (au)
Distance (μm)
B
M1-GFP
Mito mCherry
00:00
01:30
02:30
03:30
04:30
06:30
C
Overlay
Overlay
M1-GFP
TOM20
Calreticulin
D
M1-GFP
Calreticulin
TOM20
Fluorescence intensity (au)
Distance (μm)
E
M1-GFP⇨TOM20
Calreticulin⇨TOM20
M1-GFP⇨Calreticulin
n= 49 12 12
ns
***
****
Fluorescence overlap (%)
F
H
Mp
ER
MAM
Cyt
IB:spastin
IB:SigmaR1
IB:IP3R3
IB:VDAC
IB:CytC
IB:β-Tubulin
HeLa cells
Mouse brain
Mouse liver

Figure 1. Spastin partially colocalizes with mitochondria and accumulates in MERCs

(A) Representative images of HeLa cells cotransfected with M1-GFP (green) and mito-mCherry (red) and relative fluorescence intensities for the indicated linear regions measured by line scan analysis along the mito-mcherry staining (dotted lines in magnified inbox, overlay). Arrows indicate representative overlaps between M1-GFP puncta and mitochondria. Scale bar, 10 μm.

(B) Representative live-cell image of HeLa cells expressing M1-GFP (green) and mito-mCherry (red). Time-lapse images of boxed area reveal interaction between M1-GFP puncta (arrows) and dynamic mitochondrion over the entire video. Time is indicated in min:sec. Scale bar, 10 μm.

(C) HeLa cells were transfected with M1-GFP, fixed, and then stained for TOM20 and calreticulin to visualize mitochondria and ER, respectively. Arrows in the inbox indicate representative overlaps between M1-GFP puncta, ER, and mitochondria. Scale bar, 10 μm.

(D) Line scan analysis of the intensity fluorescence along the TOM20 staining (dot line in the overlay inbox) reveals partial overlaps between mitochondria, ER, and M1-GFP.

(E) Quantification of the overlap as percentage between M1-GFP and TOM20 or calreticulin and TOM20 or M1-GFP and calreticulin staining. Data are shown as mean ± SEM. One-way ANOVA Tukey's multiple comparisons test. ***$p < 0.005$; ****$p < 0.001$; ns, not significant. n, number of cells analyzed.

(F) Immunoblots of subcellular fractions isolated from HeLa cells, mouse brain, or mouse liver tissues. The following markers were used: IP3R3 for the ER, VDAC1, and cytochrome *c* (Cyt C) for mitochondria (Mp, mito pure), SigmaR1 for MAMs (MERCs), and β-tubulin for cytosol (Cyt). H: homogenate. All markers were enriched in their respective compartments. The close apposition between ER and mitochondria membranes at MAMs explained the presence of both VDAC1 and IP3R3 in these microdomains.

In cells ER occupies a large fraction of the cytoplasmic volume, and its membrane establishes functional connections without membrane fusion with several intracellular organelles named membrane contact sites (MCSs).[20,21] MCSs between ER and mitochondria, namely MERCs (mitochondria-ER contacts) or MAMs (mitochondria-associated membranes), cover 4% to 20% of mitochondrial surface area depending on the cell type and their metabolic state.[22] MERCs allow mitochondria to communicate directly with ER and regulate essential cellular processes such as calcium (Ca^{2+}) signaling, phospholipid exchange, intracellular trafficking, ER stress, ER proteostasis, and autophagy.[23–25] Several studies suggested that the disturbance of MERCs occur in major neurodegenerative disease including HSP.[26,27] Indeed, REEP1, RTN2, and atlastin-1, three HSP-linked ER-shaping proteins to which M1 spastin interacts, have been implicated to MERCs homeostasis.[28] The role of spastin in MERCs and mitochondria functions is to date by far less understood. During the past years, defective spastin expression was associated with altered mitochondrial trafficking in neurites of SPG4-HSP cellular models, likely explained by changing in post-translational modifications (PTMs) of tubulin.[29–32] Only recently the lack of spastin was associated with impaired mitochondrial morphology and functions,[33–35] and a deregulation in the number of MERCs was observed in a Zebrafish model overexpressing M1-spastin.[18]

In the present study, we aimed at elucidating the potential role of spastin in ER-mitochondria contact sites and mitochondria-related functions. We provide data that support the localization of spastin in MERCs and show that defect in SPG4 expression leads to an increased number of MERCs, altered mitochondria morphology, lower mitochondria and ER Ca^{2+} content, and downregulation of oxidative metabolism in cells.

RESULTS

Spastin localizes in mitochondrial-ER contact sites

To visualize the intracellular localization of the full-length isoform of spastin, we first transfected HeLa cells with Flag- or GFP-tagged forms of either wild-type M1-spastin (M1) or a form of the protein carrying the C448Y (C445Y in mice) mutation (M1CY).[16,36] Overexpressed M1 showed a typical perinuclear distribution with discrete puncta, whereas the enzymatically inactive M1CY had a puncta-filamentous pattern that decorated and bundled a subset of MTs that extensively colocalize with ER, as previously described[16,36,37] (Figures 1A–1C and S1). The M1CY variant allows to visualize M1 intracellular localization while preventing a potential ER shrinking due to the MT-severing activity of WT-M1 spastin. To verify whether M1-spastin partially colocalizes with mitochondria, cells were cotransfected with mito-mCherry or stained with antibodies against the outer mitochondrial membrane (OMM) proteins TOM20 or TOM40, and the fluorescence intensity of the probes was measured by line scan analysis over the length of the longer mitochondria (Figures 1A and S1). Representative line scans revealed that M1-spastin partially overlap with mitochondria regardless of the tag and the form of M1-spastin. To evaluate the dynamic localization of M1 puncta relative to mitochondria, we imaged live HeLa cells cotransfected with M1-GFP and mito-mCherry (Figure 1B and Video S1). In HeLa cells, mitochondria exist prevalently as tubules of different length, but globular and ring-shaped structure can be also observed. Most of the mitochondria visualized in Video S1 constantly changed the morphology, and their dynamics range from being relatively static over time to moving rapidly. Of the 213 M1-GFP puncta analyzed, 91.5% remained static with minimal two-dimensional fluctuation over the entire time-lapse video. In these cells, 15.70% ± 1.8% of M1-GFP overlaps transiently with mito-mCherry-labeled mitochondria. Some M1-GFP puncta-mitochondria interactions (Video S1, Figure 1B Insets) were stable over time, with dynamic mitochondria moving mostly behind M1 particles. However, we did not observe fission or fusion events at the crossing points between M1 spastin and mitochondria at the time resolution of our experimental conditions. Costaining of TOM20 and the ER luminal protein calreticulin in cells expressing M1-GFP or M1CY-GFP further revealed puncta of colocalization of these three compartments, suggesting that M1-spastin may localize in ER-mitochondria contact sites (Figures 1C, 1D, S1E, and S1F). To quantify the extent of M1-overexpressed proteins that colocalize with mitochondria or ER, we quantified the overlap, as percentage, between M1-GFP (or M1CY-GFP) and TOM20 or calreticulin staining, respectively (Figures 1E and S1G). We found that M1 proteins extensively overlap calreticulin staining with 48.1% ± 13.3% and 72% ± 14% (mean ± SEM) for M1 and M1CY, respectively, confirming previous results[16] and the ER localization of M1 isoforms. The two forms of M1 displayed also a significantly overlap with TOM20 staining with 23.3% ± 10% and 36.4% ± 8%, for M1 and M1CY, respectively. For comparison, in both cases, ~29% of total calreticulin staining overlap TOM20 (Figures 1E and S1G), which is comparable with the values obtained for M1 and M1CY as ER-membrane proteins. Similar results were obtained measuring the overlap

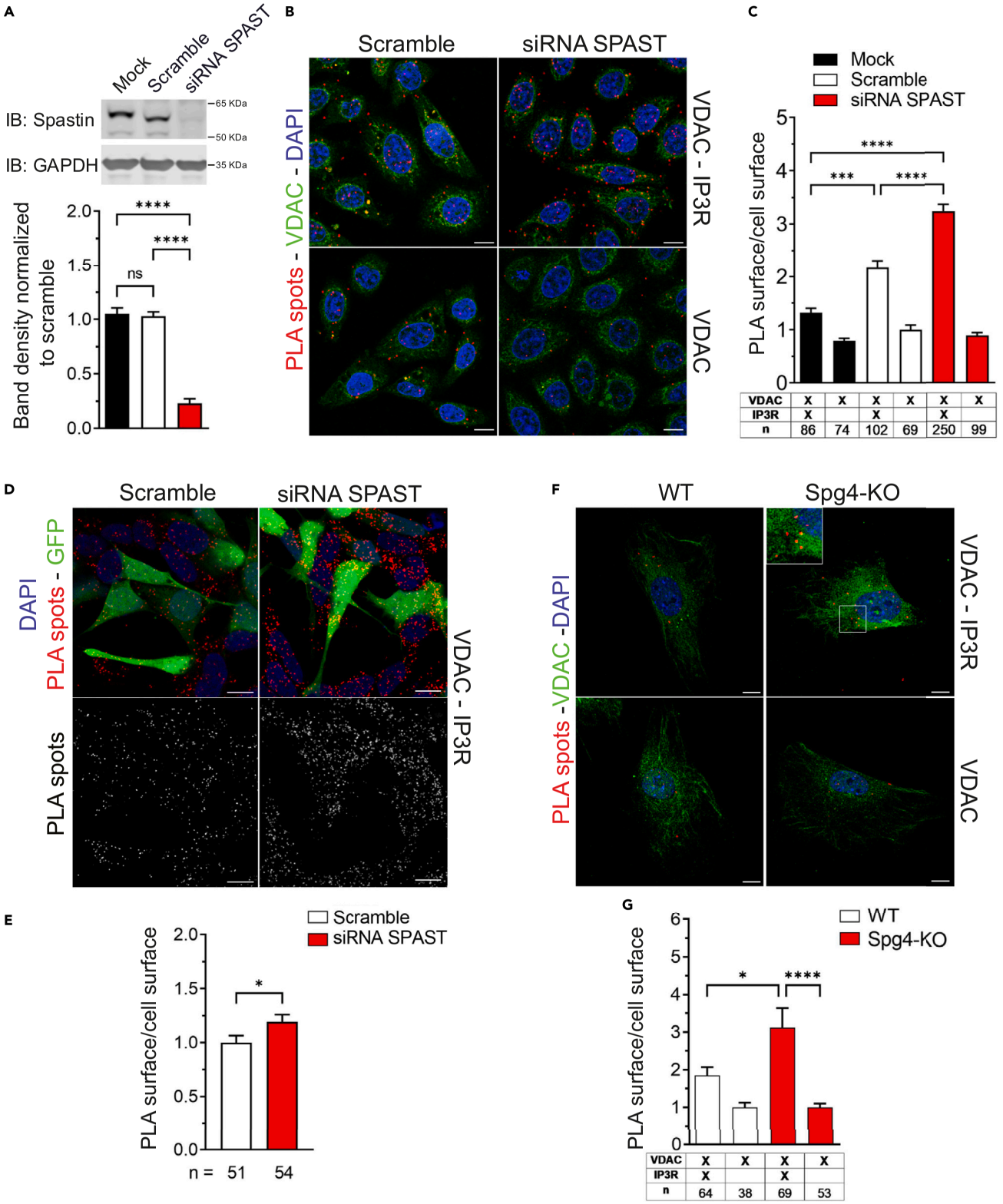
A
Mock
Scramble
siRNA SPAST
IB: Spastin
IB: GAPDH
65 KDa
50 KDa
35 KDa
Band density normalized to scramble
ns
****
****
B
Scramble
siRNA SPAST
PLA spots - VDAC - DAPI
VDAC - IP3R
VDAC
C
Mock
Scramble
siRNA SPAST
PLA surface/cell surface
***
****
****
VDAC X X X X X X
IP3R X X X
n 86 74 102 69 250 99
D
Scramble
siRNA SPAST
DAPI
PLA spots - GFP
PLA spots
VDAC - IP3R
E
Scramble
siRNA SPAST
PLA surface/cell surface
*
n = 51 54
F
WT
Spg4-KO
PLA spots -VDAC -DAPI
VDAC - IP3R
VDAC
G
WT
Spg4-KO
PLA surface/cell surface
*
****
VDAC X X X X
IP3R X X
n 64 38 69 53

Figure 2. Depletion of spastin increases the number of MERCs

(A–C) HeLa cells were mock transfected or treated with scramble or siRNA SPAST for 72 h. Cells were then lysed or fixed and processed for WB and PLA, respectively.

(A) Representative immunoblot of protein extracts for spastin and GAPDH and quantification of the band densities normalized to both GAPDH and scramble condition.

(B) Cells were costained for VDAC1 (cat# ab15895) and IP3R (cat# 610312, upper panels) or labeled only for VDAC1 (bottom panels) as control. Cells were then processed for PLA as described in MM.

(C) Quantification of the surface of PLA-positive spots per surface of the cell. Data are normalized to scramble condition stained only with VDAC1.

(D) SH-SY5Y cells were treated twice with scramble or siRNA SPAST for 72 h and then fixed and processed for PLA. SH-SY5Y cells were cotransfected with GFP to better visualize their morphology. Cells were costained for VDAC1 (cat# ab14734) and IP3R (cat# ab5804).

(E) Quantification of the surface of PLA-positive spots in GFP-positive cell per area of each cell shown in (D). Data are normalized to scramble condition.

(F) Mouse embryonic fibroblasts from WT or Spg4-KO mice were fixed, costained for VDAC1 (cat# ab15895) and IP3R (cat# 610312, upper panels) or labeled only for VDAC1 (bottom panels) and processed for PLA.

(G) Quantification of the surface of PLA signal per area of each cell shown in (F). Data are normalized to WT fibroblasts stained only with VDAC1. Data are shown as mean ± SEM. One-way ANOVA Tukey' or Sidak's multiple comparisons test. *$p < 0.05$; ***$p < 0.005$; ****$p < 0.001$; ns, not significant. n, number of cells analyzed. Scale bars, 10 μm.

between the GFP-tagged ER membrane protein ATF6 and mito-mCherry to label mitochondria (31.2% ± 8.4%, not shown). In parallel, to analyze whether the above-described localization of spastin, where the ER tubules crossed mitochondria, corresponds to mitochondria-ER contact sites, we performed subcellular fractionation analyses of HeLa cells, mouse brain, and liver tissues.[38] Consistently, we revealed a previously unknown localization of endogenous spastin at mitochondria-ER contact sites as shown by its detection in the MAM fraction of these analyzed samples (Figure 1F).

Taken together, these data support the hypothesis that the full-length isoform of spastin localizes in ER-mitochondrial contact sites.

Spastin regulates the number of MERCs

MERCs are involved in several cellular functions, and alteration in their number has been already associated with different neurodegenerative diseases including HSP.[27,28,39] To investigate whether a reduced expression of spastin may affect the number of MERCs, we used proximity ligation assay (PLA)[40] in HeLa cells silenced by siRNA against spastin (siRNA SPAST). Mock and scramble siRNA transfection were used as control conditions. Efficiency of silencing of endogenous spastin was assessed by immunoblot (Figures 2A, S3C, and S3D) and RT-qPCR analysis (not shown) with an average reduction of 80% and 85% for its expression and transcript, respectively. To visualize MERCs, we used VDAC1 and IP3R as probes for mitochondria and ER, respectively, as previously shown.[41,42] Cells were labeled with the two antibodies to visualize ER-mitochondria contact sites or just one (VDAC1) to monitor the background signal (Figure 2B). Quantification of total PLA surface per area of each cell showed that spastin silencing significantly increased the number of PLA signal compared to scramble and mock transfected cells (Figure 2C). To further confirm these results, we analyzed the number of MERCs both in SH-SY5Y cells and in primary mouse embryonic fibroblasts (MEF) obtained from Spg4-KO mice as well as WT control. SH-SY5Y is a human neuroblastoma cell line commonly used as neuronal *in vitro* model to study neurodegenerative disorders,[43,44] which has been also used recently in the context of SPG4-HSP disease.[45–47] Spastin expression level in SH-SY5Y and Spg4-KO MEF was quantified by immunoblot with an average reduction of 66% and ~100%, respectively (Figures S2A, 3C, and 3D). Similarly to HeLa cells, PLA signal was significantly detectable in SH-SY5Y only in the presence of the two antibodies VDAC1 and IP3R (Figure S2B), and a significant increase of PLA signal was found both in spastin-silenced SH-SY5Y cells (Figures 2D and 2E) and Spg4-KO MEF (Figures 2F and 2G) compared to control conditions. Taken together these results indicate an increased number of MERCs in spastin defective and Spg4-KO cell models.

Spastin-dependent MERCs deregulation is not related to MT dynamics

Although MTs are dispensable for the formation of ER network, they regulate its intracellular distribution and the ER sheet/tubule balance.[48,49] In animal cells, ER movement along MTs depends mainly on two different mechanisms named sliding and tip attachment complex (TAC).[50] Sliding occurs preferentially on acetylated MTs,[51] a PTM of tubulin associated with stable long-lived MTs[52] and already found increased in different spastin defective cellular models.[16,29,32,33,53] Interestingly, it has been suggested that ER sliding on acetylated MTs provides a mechanism to establish or maintain ER-mitochondria contact sites.[51] Thus, an increased level of acetylated tubulin in our SPG4 defective cell models might explain the observed increased number of MERCs. To assess this hypothesis, we quantified the protein expression levels of β-tubulin to measure the extent of the total mass of tubulin and the levels of acetylated- and tyrosinated-α-tubulin, to quantify the long-lived and the dynamic MTs, respectively.[54] As shown in Figure 3, in spastin-silenced HeLa cells and Spg4-KO MEF, neither immunoblot analysis on HeLa cells (Figures 3A and 3B) and fibroblasts (Figures 3C and 3D) nor the quantification of acetylated/tyrosinated tubulin ratio by immunofluorescence (Figures 3E and 3F) showed significative differences in the tubulin mass and the PTMs of tubulin analyzed in agreement with previous observations.[55]

To further investigate whether spastin's regulation of ER-mitochondrial contact sites depends merely on the presence of M1-spastin or also on its MT-severing activity, we overexpressed a murine GFP-tagged M1-spastin (M1-GFP) or the enzymatically inactive forms of this protein in spastin-silenced HeLa cells, which showed an increased number of MERCs (Figures 2B and 2C). Particularly, we used M1CY-GFP or M1RC-GFP harboring two different pathological missense mutations within the AAA domain[16,36,56] or an M1 lacking the entire AAA cassette

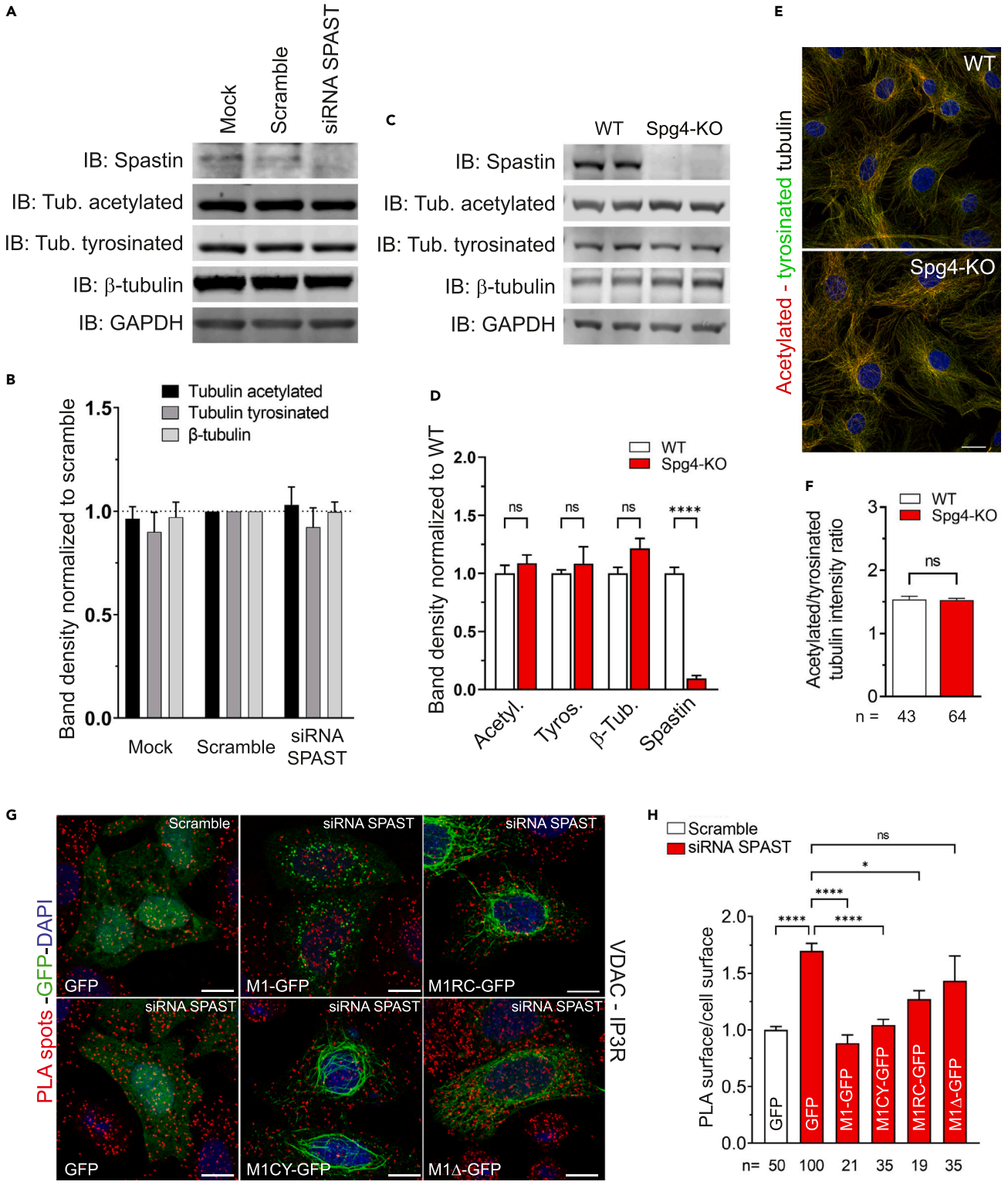

Figure 3. MERCs deregulation in spastin-lacking cells does not correlate with altered microtubule dynamics

(A) HeLa cells were mock transfected or treated with scramble or siRNA SPAST for 72 h as described in MM, then their protein extracts were analyzed by immunoblot.

(B) Quantification of the band densities in (A). Data are normalized to GAPDH and scramble conditions. No significant statistical difference was observed.

Figure 3. *Continued*

(C–F) Spg4-KO or WT MEF were cultured, and proteins were extracted and analyzed by immunoblot (C and D) or cells were fixed and costained for acetylated (red) and tyrosinated (green) tubulin (E and F). Scale bar, 20 μm. (D) Quantification of the band densities of the immunoblot in (C). Data were normalized to both GAPDH and WT signal. (F) Ratio between acetylated and tyrosinated average fluorescence intensities measured for each cell in (E).

(G) HeLa cells were treated with scramble or siRNA SPAST for 48 h, then transfected with GFP-tagged full-length mouse spastin M1 (M1-GFP) or mutated forms of the protein (M1CY-GFP, M1RC-GFP, or M1Δ-GFP), fixed after 24 h and finally processed for PLA using VDAC1 (cat# ab14734) and IP3R (cat# ab5804) antibodies. Scale bars, 10 μm.

(H) Quantification of PLA surface spots in GFP-positive cells per area of each cell shown in (G). Data are normalized to scramble condition. Data are shown as mean ± SEM. One-way ANOVA Tukey's multiple comparisons test for (B), (D), and (H), unpaired Student's t test for (F). *$p < 0.05$; ****$p < 0.001$. ns, not significant. n, number of cells analyzed.

(aa 1–338; M1Δ-GFP) as previously described.[16] As shown in Figures 3G and 3H, the overexpression of M1, M1CY, and M1RC, but not that of M1Δ, significantly rescued the PLA signal to basal level (scramble), demonstrating not only that the increased number of MERCs here observed depends on the presence of a full-length isoform of spastin but also that its MT-severing activity is dispensable.

Taken together, these results suggested that the effects of M1-spastin on MERCs regulation are independent on MT dynamics and spastin-severing activity.

Spastin alters mitochondria morphology but not their mass

The functions and the health of mitochondria are intimately linked to their morphology,[57] and the processes of fission and fusion that shaped this organelle are spatially coordinated at MERCs.[58–61] Indeed, an altered number of ER-mitochondria contact sites might be associated with changing in mitochondria morphology and mass. To analyze these cell parameters, HeLa cells were silenced as described above and stained for TOM20 to quantify the size of mitochondria. After images segmentation (see method details) morphometric analysis of TOM20 staining revealed a significant increase in mitochondrial/cell surface ratio in spastin-silenced HeLa cells compared to control condition (Figures 4A and 4B). Accordingly, analysis of mitochondria morphology performed by transmission electron microscopy (TEM) showed a significant increase in the length and/or perimeter of mitochondria in cells lacking spastin (Figures 4C and 4D). Interestingly, these mitochondria showed normal cristae but often altered donut-shaped form, a morphological feature of mitochondrial dysfunction associated with loss of mitochondrial membrane potential.[62] However, mitochondrial mass, measured using MitoTracker green[63] by FACS in SPAST-silenced HeLa cells (Figures S3A and S3B) or by video-imaging in Spg4-KO MEF (Figure 7F), was unchanged compared to control conditions. In agreement with these results, the expression levels of several OMM and inner mitochondrial membrane (IMM) proteins, but also that of the mitochondrial fission protein Drp1[64] and its phosphorylated form (Ser616), were not significantly affected in cells lacking spastin (Figures S3C and S3D).

Spastin modulates Ca^{2+} homeostasis, reactive oxygen species levels, mitochondrial membrane potential, and oxidative phosphorylation

The ER is the major intracellular Ca^{2+} store in cells, and MERCs are involved in Ca^{2+} transfer from ER stores to mitochondria via a transfer machinery complex composed of IP3R at the ER membrane, GRP75, and the voltage-dependent anion channel (VDAC) at the OMM.[24] Ca^{2+} transferred via VDAC moved to the mitochondrial matrix via the mitochondrial Ca^{2+} uniporter (MCU) situated on the IMM. In mitochondria, Ca^{2+} regulates several enzymes involved in ATP synthesis and the related oxygen consumption rate.[65–67] Correlation between dysregulation of MERCs and Ca^{2+} homeostasis has been already observed in several diseases.[39,68–70] Considering the observed alteration of MERCs number, we thus examined the effect of spastin deletion on Ca^{2+} dynamics in different subcellular compartments using recombinant aequorin probes.[71] A striking difference (~20%) was evident in $[Ca^{2+}]_{er}$ (Ca^{2+} concentration within ER lumen) steady-state levels in spastin-silenced HeLa cells compared to their control (Figure 5A). In agreement with the $[Ca^{2+}]_{er}$ data, the $[Ca^{2+}]$ increases evoked by agonist stimulation (histamine, His) in the cytosol and the mitochondria were significantly lower (~29% and ~25% reduction of Ca^{2+} response in cytosol and mitochondria, respectively) after spastin deletion compared to control condition (scramble) (Figures 5B and 5C). Similar effects were observed in the SH-SY5Y cells where ER (~20%), cytosolic (~34%), and mitochondria (~48%) $[Ca^{2+}]$ are deeply altered after spastin deletion (Figures 5D–5F). Finally, the effect of spastin deletion on Ca^{2+} levels was also confirmed in Spg4-KO fibroblasts compared to WT, indicating a significant reduction of ~38%, ~21%, and ~24% for ER, cytosol, and mitochondria, respectively (Figures 5G–5I).

Mitochondria respiration is considered the major source of cellular reactive oxygen species (ROS), and MERCs are enriched in redox-regulatory proteins.[72–74] It is also widely accepted that mitochondrial matrix $[Ca^{2+}]$ regulates mitochondrial respiration and ROS-generating enzymes activity.[75,76] To estimate the mitochondrial ROS level in live HeLa cells and fibroblasts, we used the mitochondrion-targeted probe MitoSOX at low concentration.[77] Cells were analyzed by live imaging or by FACS. Figures 6A and 6B shows that downregulation of spastin in HeLa cells significantly reduced the level of ROS, whereas antimycin A treatment, an inhibitor of complex III of respiratory chain, induced a marked increase of MitoSOX fluorescence, as expected. A decreased MitoSOX fluorescence intensity level was also observed in Spg4-KO MEF compared to WT both by live imaging (Figures 6C and 6D) and by FACS (Figures 6E and 6F) but not in spastin-silenced SH-SY5Y cells (not shown).

Mitochondrial ROS level and $[Ca^{2+}]$ are also intimately linked to mitochondrial membrane potential ($\Delta\Psi m$). Indeed, a strong positive correlation exists between $\Delta\Psi m$ and ROS, and it is widely accepted that mitochondria produce more ROS at high $\Delta\Psi m$.[78–80] In addition, cytoplasmic Ca^{2+} enters the mitochondrial matrix via the MCU channel pore driven by electrochemical gradient provided by $\Delta\Psi m$. Interestingly, decreased $\Delta\Psi m$ in aged cells inhibits uptake of Ca^{2+} by mitochondria.[81] To assess whether the level of spastin regulates $\Delta\Psi m$, the same

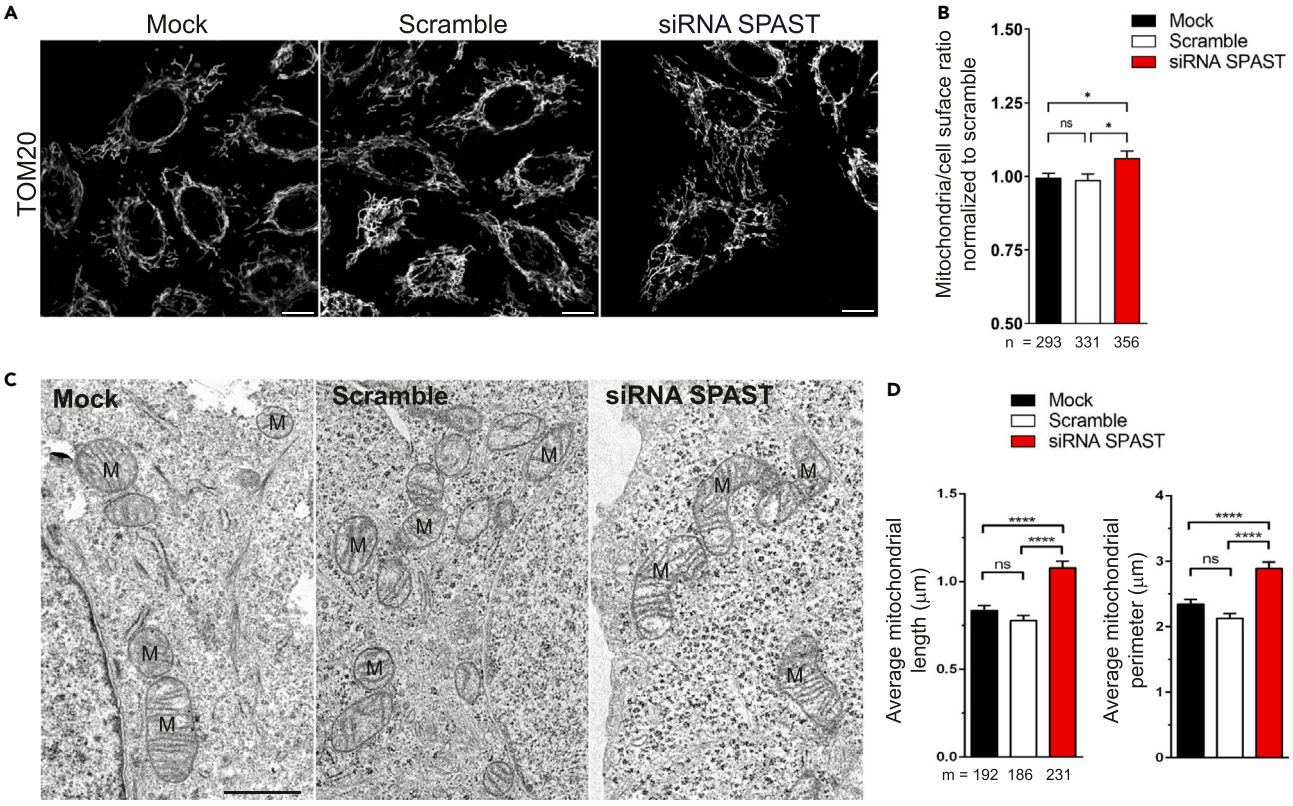

Figure 4. Decreased spastin expression alters mitochondria morphology

(A–D) HeLa cells were mock transfected or treated with scramble or siRNA SPAST for 72 h, then fixed and stained for TOM20 (A and B) or processed for transmission electronic microscopy (C and D). (A) Representative images of HeLa cells treated with siRNA, fixed and stained for TOM20. Scale bars, 10 μm. (B) Images in (A) were segmented as described in MM, and the total mitochondrial surface was quantified and normalized by the surface of each cell. (C) Representative TEM images of HeLa cells treated with siRNA. Scale bar, 1 μm. (D) Quantification of both the average length (major axis of the equivalent ellipse) and the perimeter of mitochondria (M) in (C). Data are shown as mean ± SEM. One-way ANOVA Dunnett's or Tukey's multiple comparisons test. *$p < 0.05$; ****$p < 0.001$; ns, not significant. n, number of cells analyzed. m, number of mitochondria analyzed.

cellular models described above were incubated with the fluorescent lipophilic cationic dye TMRM or the ratiometric $\Delta\Psi$m indicator JC-1.[82] As for ROS analysis, the fluorescence intensities of these dyes were analyzed by live imaging or via FACS. Cells were treated, or not, with the proton ionophore FCCP to induce a sharp dissipation of $\Delta\Psi$m. As shown in Figures 7A and 7B, a slight but significant reduction of TMRM signal was observed in spastin-silenced HeLa cells compared to controls, whereas 10-μM FCCP totally dissipated the signal. Comparable results were obtained in spastin-silenced HEK cells incubated with JC-1 and analyzed by FACS where a significant decrease of red/green ratio indicates a reduction of $\Delta\Psi$m (Figure S4). Similarly, spastin-silenced SH-SY5Y cells (Figures 7C and 7D) and Spg4-KO MEF (Figures 7E and 7F) showed a significant reduction of TMRM fluorescence intensity compared to control conditions. In MEF experiments, cells were also coincubated with MitoTracker green whose intensity is independent on changing of $\Delta\Psi$m, as demonstrated by its unaltered fluorescence levels after FCCP treatment (Figure 7F).

To further analyze the role of spastin on mitochondrial functions, we analyzed the oxidative phosphorylation (OXPHOS) by measuring mitochondrial oxygen consumption rate (OCR) in WT and Spg4-KO MEF using the Seahorse bioanalyzer[83,84] (Figure 8A). Comparison between two different WT and two different Spg4-KO MEF lines revealed a statistically significant reduction of ATP-linked production and maximal or basal respiration in the absence of spastin, whereas spare respiratory capacity showed a reduced trend that is not always significant between the WT and Spg4-KO samples analyzed (Figure 8B). On the other hand, other parameters such as proton leak and coupling efficiency are unaffected in the same experimental conditions (not shown). To investigate the role of spastin on the energetic status in this cellular model, we compared total ATP levels in total cell lysates from four different Spg4-KO and four different WT MEF lines as described in MM. Our data demonstrate that there are no significant differences in the total ATP levels between WT and mutant cells (Figure 8C), suggesting a compensatory upregulation of glycolysis in Spg4-KO cells.

Taken together, these data show that spastin depletion globally affects Ca^{2+} signaling, which is associated with reduced mitochondrial membrane potential and partially ROS levels. In addition, mitochondrial stress test revealed downregulation of mitochondrial respiration in Spg4-KO fibroblasts, suggesting an overall dysregulation of mitochondrial metabolism.

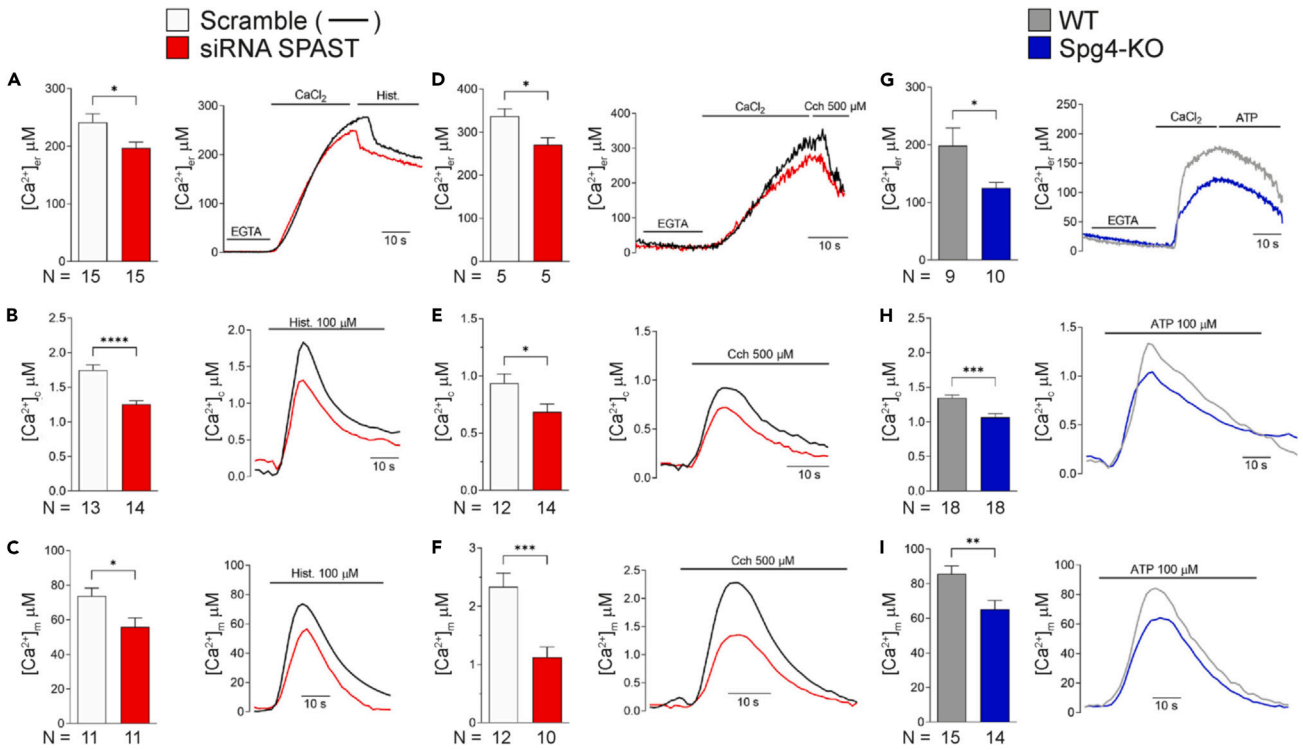

Figure 5. Ca^{2+} dysregulation in spastin-deficient cells

(A–C) Kinetics of reticular (A), cytosolic (B), and mitochondrial (C) Ca^{2+} in HeLa cells treated with scramble or siRNA SPAST for 72 h. Where indicated, recombinant aequorin-transfected cells were treated with 100 µM histamine (Hist). Reticular Ca^{2+} concentration ($[Ca^{2+}]_{er}$) peaks: scramble 241.49 ± 15.35, siRNA SPAST 196.71 ± 11.07; cytosolic Ca^{2+} concentration ($[Ca^{2+}]_c$) peaks: scramble 1.74 ± 0.078, siRNA SPAST 1.25 ± 0.05; mitochondrial Ca^{2+} concentration ($[Ca^{2+}]_m$ peaks: scramble 73.79 ± 4.60, siRNA SPAST 55.77 ± 5.33.

(D–F) Experiments analogous to (A–C) were carried out in SH-SY5Y cells. In these cells, the agonist used was 500 µM carbachol (Cch). $[Ca^{2+}]_{er}$ peaks: scramble 337.2 ± 17.35, siRNA SPAST 271.2 ± 15.90; $[Ca^{2+}]_c$ peaks: scramble 0.936 ± 0.080, siRNA SPAST 0.686 ± 0.068; $[Ca^{2+}]_m$ peaks: scramble 2.33 ± 0.237, siRNA SPAST 1.123 ± 0.181.

(G–I) Measurements of $[Ca^{2+}]$ using recombinant aequorin upon agonist stimulation (100 µM ATP) in MEF from WT or Spg4-KO mice. $[Ca^{2+}]_{er}$ peaks: WT 198.41 ± 32.73, Spg4-KO 124.94 ± 10.39; $[Ca^{2+}]_c$ peaks: WT 1.34 ± 0.048, Spg4-KO 1.06 ± 0.06. $[Ca^{2+}]_m$ peaks: scramble 85.58 ± 4.77; Spg4-KO 65.22 ± 5.28. Data are shown as mean ± SEM. Unpaired Student's t test. *$p < 0.05$; **$p < 0.01$; ***$p < 0.005$; ****$p < 0.001$; N, number of experiments analyzed.

DISCUSSION

The longest isoform of spastin, M1, spans the outer leaflet of ER membrane, and it is likely enriched in the tubular region of ER network[7] where contacts with mitochondria are more common.[61] Mutations of this isoform have been regarded as the most pathogenic for HSP, because M1 is found enriched in the spinal cord of adult rodents,[85] the site of the main pathological histological feature of SPG4-HSP, i.e., the axonal swellings, and because of its interaction with other HSP and ER-morphogens proteins such as Atlastin-1, REEP1, and reticulums. However, there is currently no scientific evidence to suggest a cause-and-effect link between spastin-dependent ER alterations and the onset of the disease.

In this work, we show that ~20% of overexpressed M1-spastin overlaps with mitochondria in HeLa cells, which agrees with the results obtained for other ER proteins. Moreover, we observed puncta of colocalization between ER, mitochondria, and M1, suggesting that spastin localizes also in MERCs. This assumption was supported by membrane fractionation analysis where we found that endogenous spastin localizes and accumulates in MERC fraction and by the fact that the expression level of spastin affects the number of MERCs in different cell models including the neuroblastoma SH-SY5Y cell line. Analysis of mitochondrial functions linked to MERCs homeostasis revealed that the reduction of spastin expression impairs mitochondrial but also ER Ca^{2+} content, and this is associated with a decreased $\Delta\Psi m$ and partially the ROS levels, suggesting a metabolic mitochondrial dysregulation. Indeed, maximal mitochondrial respiration and ATP-linked production are significantly affected in Spg4-KO fibroblasts, supporting these conclusions. In addition, we observed changes in mitochondria morphology that appear longer and often with a donut-like shape.

To date the role of spastin in MERCs and mitochondrial homeostasis is nearly unexplored. Nevertheless, some recent data are consistent with our observations. For instance, in Drosophila model carrying a pathogenic missense mutation of spastin, the ER Ca^{2+} content is reduced.[19] The authors suggested that this effect depends on the impairment of store-operated Ca^{2+} entry (SOCE), the mechanism necessary for ER Ca^{2+} reuptake after ER-store depletion.[86] SOCE was also found impaired in iPSC-derived cortical neurons from SPAST patients, which is likely due to an altered MT-dependent traffic of STIM1 to plasma membrane.[17] About the role of spastin on mitochondrial morphology and

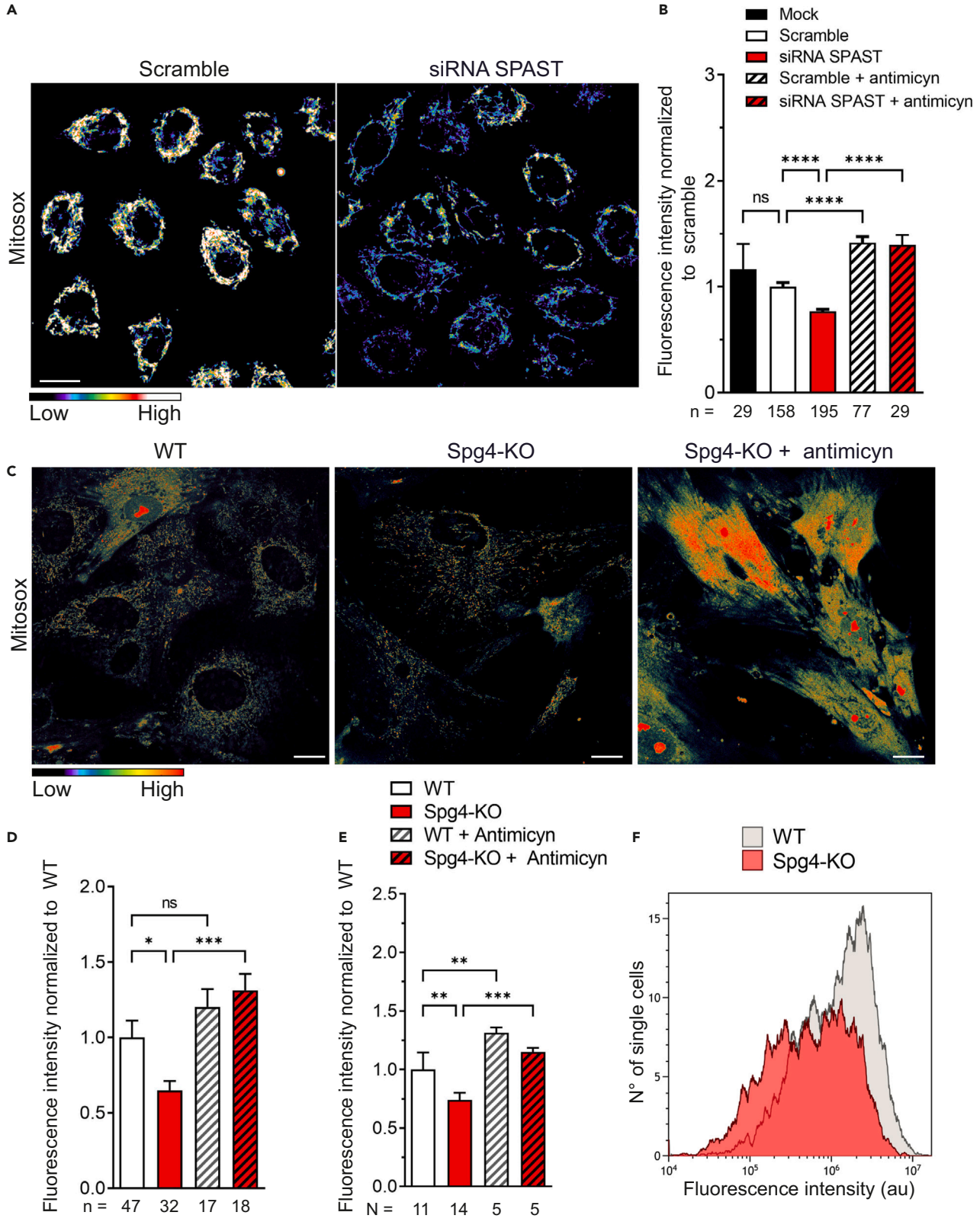
A
Scramble
siRNA SPAST
Mitosox
Low
High
B
Mock
Scramble
siRNA SPAST
Scramble + antimicyn
siRNA SPAST + antimicyn
Fluorescence intensity normalized to scramble
ns
****
****
****
n = 29 158 195 77 29
C
WT
Spg4-KO
Spg4-KO + antimicyn
Mitosox
Low
High
D
Fluorescence intensity normalized to WT
ns
*
***
n = 47 32 17 18
E
WT
Spg4-KO
WT + Antimicyn
Spg4-KO + Antimicyn
Fluorescence intensity normalized to WT
**
**
***
N = 11 14 5 5
F
WT
Spg4-KO
N° of single cells
Fluorescence intensity (au)

Figure 6. Reduction of spastin expression impairs ROS production

(A and B) HeLa cells were mock transfected or treated with scramble or siRNA SPAST for 72 h. Cells were then incubated with 2.5 μM MitoSOX for 30 min and imaged live. Cells were then incubated with 20 μM antimycin A for 10 min to induce ROS production.

(C–F) Mouse fibroblasts from WT or Spg4-KO mice were loaded with 2.5 μM MitoSOX for 30 min and imaged live (C and D) or processed by FACS (E and F). Cells were then incubated with 20 μM antimycin A for 10 min to induce ROS production. Data are shown as mean ± SEM. One-way ANOVA Sidak's multiple comparisons test. *$p < 0.05$; **$p < 0.01$; ***$p < 0.005$; ****$p < 0.001$; ns, not significant. n, number of cells analyzed. N, number of experiments analyzed. Scale bars, 10 μm. In (A) and (C), MitoSOX fluorescence intensity is shown as pseudo colors.

oxidative metabolism, data are more contradictory, likely dependent on the experimental approach and the cell model analyzed. Indeed, in SPAST patient-derived fibroblasts, Dong et al. found a decreased $\Delta\Psi$m associated with a reduced ATP content and a mitochondrial fragmentation,[34] whereas in a similar cell model but large-scale machine-learning-based study, Wali et al. revealed an increased mitochondrial size.[33] On the other hand, in SPAST-patient-derived ONS cells, the same research group observed a trend toward lower respiratory chain function but not other mitochondrial dysfunction.[87] M1 spastin has been already involved in MCSs between different organelles. Particularly, M1 overexpression reduced the number of MERCs in zebrafish model,[18] which agrees with our results, but also regulates MCSs between ER and lipids droplets (LD) or LD and peroxisomes.[18,88,89] LDs are cytosolic organelles storing lipids that have critical roles in lipid and energy homeostasis. LDs arise from tubular ER with which they maintain a close relationship during their lifetime, but they also established functional connections with mitochondria. Indeed, LDs seem work as power supply for mitochondria to generate ATP by OXPHOS.[90,91] In stress conditions, M1-spastin accumulates in LDs and regulates their metabolism.[89] In agreement with our observation, lack of spastin increases the number of LDs and their proximity with ER membrane,[92] suggesting a potential role of spastin in the crosstalk between ER-mitochondria and LDs.[93]

MCSs between the ER and mitochondria, which primarily occur at tubular ER, are of great importance for Ca^{2+} ion homeostasis. Indeed, several enzymes of Krebs cycles and glycolysis located in mitochondria matrix are Ca^{2+} dependent, and perturbing MERCs can decrease oxygen consumption rate and ATP production.[94] The mitochondrial Ca^{2+} uptake from ER at MERCs depends on different parameters such as MERCs distance, length, and coupling number.[95] Theoretically an increased number of MERCs should correlate with more Ca^{2+} transit from ER to mitochondria as previously reported,[96–99] which conflicts with our observations. We speculate that in our spastin-deficient cell models, the observed increased number of MERCs could be a compensatory cellular response to counterbalance the lower mitochondrial Ca^{2+} concentration. However, the simultaneous low Ca^{2+} content in the ER may prevent to achieve the resting mitochondrial Ca^{2+} concentration required for their essential cellular functions. This condition, particularly if chronic, could be implicated in the pathophysiology of HSP-SPG4 disease. Whether the reduction of $[Ca^{2+}]_{er}$ depends on a defective SOCE also in our spastin-deficient cell models remains to be explored. $\Delta\Psi$m being the driving force for mitochondrial cations uptake including Ca^{2+} and protons, its reduction likely further decreases the mitochondrial $[Ca^{2+}]$ matrix but also the proton motive force needed for the ATP synthesis. Indeed, we observed a significant reduction of OXPHOS parameters in Spg4-KO fibroblasts, particularly maximal mitochondrial respiration and ATP-linked production. However, the total ATP levels, which is the sum of ATP production rate from glycolysis and mitochondrial oxidative phosphorylation, are not significantly different between the WT and mutant cells, suggesting a compensatory upregulation of glycolysis. Finally, the altered mitochondrial morphology observed in this study might be related to the lower $\Delta\Psi$m. Indeed, mitochondrial depolarization pushes mitochondria toward fusion[59] and loss of $\Delta\Psi$m triggers mitochondrial structural changes from tubular to ring-shaped[62] that could be also dependent on mitochondrial fusion mechanism.[100]

How spastin regulates MERCs remains to be determined. Although MTs are necessary for the organization and the dynamics of both ER and mitochondria, their role in the formation and stabilization of MERCs remains largely unknown. Perhaps, the more plausible hypothesis is that the absence of spastin alters MTs dynamics, which in turn affects MERCs. Since MERCs were observed prevalently at ER tubules, a sheets-to-tubule imbalance might theoretically improve their formation. The dynamics of ER network are regulated by both MTs-dependent and MT-motor-driven movements that are under the control of tubulin code.[49,51] Though not all, several spastin defective cell models show an increased level of acetylated tubulin,[16,29,32,33,53] a PTM of tubulin associated with long-lived MTs that has been also involved in the establishment of MERCs.[51] Thus, an increased level of acetylated tubulin might increase or stabilize the association between ER and mitochondria. However, we did not observe altered levels of MTs mass or PTMs of tubulin associated with stable MTs. In addition, and within the limits of resolution of our experimental conditions, the ER morphology in spastin defective cells was indistinguishable from that of control cells (not shown) as previously observed in other SPG4-KO cell models[92] or for other ER-MT-associated proteins.[101] This hypothesis is not supported also by recent data showing that impaired spastin expression[17–19] or depletion of ER molecular partners of M1-spastin, atlastin-1[102,103] and REEP1,[104] led to a prevalence of sheet structure over tubular ER. Finally, and in agreement with this, our data demonstrated that the MT-severing activity of spastin is not required to rescue the basal level of MERCs in spastin-silenced HeLa cells, suggesting that spastin may regulate MERCs through an MT-independent process.

In conclusion, we show that in conditions mimicking the haploinsufficiency of spastin, the ER-mitochondria contact sites and mitochondria homeostasis are altered. Mitochondria being the power supply of mammalian cells, their dysregulation might be relevant for the onset or the progression of SPG4-dependent HSP.

Limitation of the study

In this work, we showed that spastin depletion increases the number of MERCs. Our results suggest that this is not related to the MT-cutting activity of spastin; however, we have not yet identified the molecular mechanism. It is possible that in spastin-deficient cells the average distance between the mitochondria and the ER is decreased, increasing the probability of MERCs being formed. This could be verified by direct visualization of spastin localization and MERCs thickness using TEM. Furthermore, it is very likely that the localization of spastin within MERCs depends on molecular partners that remain to be identified. Another limitation is that we did not further analyze why the total ATP levels are

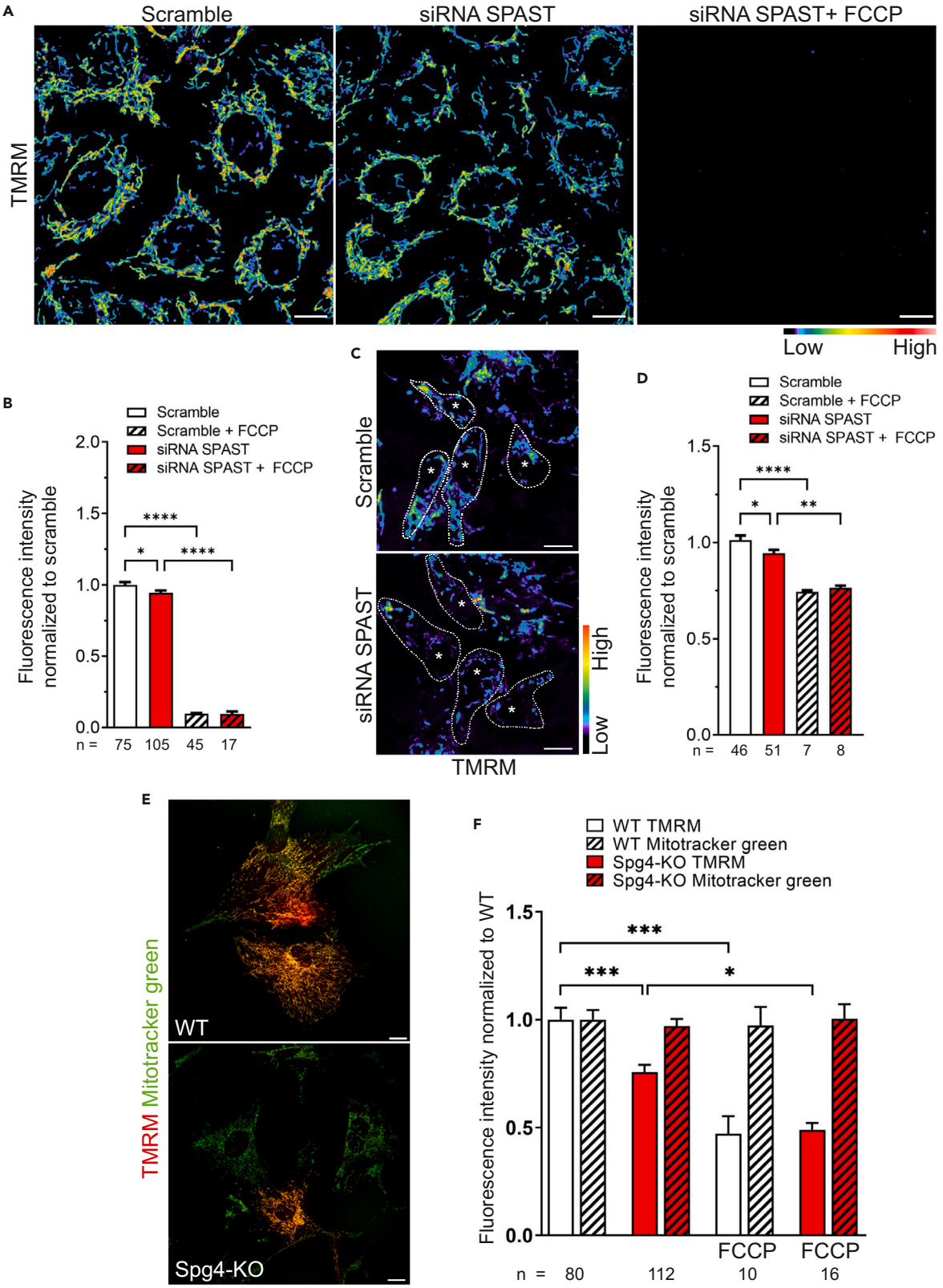
A
Scramble
siRNA SPAST
siRNA SPAST+ FCCP
TMRM
Low
High
B
Scramble
Scramble + FCCP
siRNA SPAST
siRNA SPAST + FCCP
Fluorescence intensity normalized to scramble
2.0
1.5
1.0
0.5
0.0
****
*
****
n = 75 105 45 17
C
Scramble
siRNA SPAST
High
Low
TMRM
D
Scramble
Scramble + FCCP
siRNA SPAST
siRNA SPAST + FCCP
Fluorescence intensity normalized to scramble
1.5
1.0
0.5
0.0
****
*
**
n = 46 51 7 8
E
TMRM Mitotracker green
WT
Spg4-KO
F
WT TMRM
WT Mitotracker green
Spg4-KO TMRM
Spg4-KO Mitotracker green
Fluorescence intensity normalized to WT
1.5
1.0
0.5
0.0
***
***
*
FCCP
FCCP
n = 80 112 10 16

Figure 7. Mitochondrial membrane potential ($\Delta\Psi m$) is decreased in spastin-deficient cells

(A and B) HeLa or SH-SY5Y (C and D) cells were treated with scramble or siRNA SPAST for 72 h and then incubated for 30 min with 100 nM or 400 nM TMRM, respectively. Cells were imaged live at resting conditions and then treated with 10 μM FCCP to induce dissipation of $\Delta\Psi m$. Scale bars, 10 μm; *, nuclei. Dotted lines show typical analyzed cells. TMRM fluorescence intensity is shown as pseudo colors. (B and D) Quantification of TMRM fluorescence intensity shown in (A and C).

(E and F) WT or Spg4-KO MEF were coincubated for 30 min with 100 nM TMRM and 100 nM MitoTracker green and imaged live for 15 min. Scale bars, 20 μm. Note that MitoTracker green fluorescence intensity is unaffected between WT and Spg4-KO MEF and by 10 μM FCCP treatment. Data are shown as mean ± SEM. One-way ANOVA Sidak's multiple comparisons test. *$p < 0.05$; **$p < 0.01$; ***$p < 0.005$; ****$p < 0.001$. n, number of cells analyzed.

unchanged between WT and spastin mutant cells. This suggests a compensatory upregulation of glycolysis in Spg4-KO cells, which remains to be verified and will be part of future studies.

STAR★METHODS

Detailed methods are provided in the online version of this paper and include the following:

- KEY RESOURCES TABLE
- RESOURCE AVAILABILITY
  - Lead contact
  - Materials availability
  - Data and code availability
- EXPERIMENTAL MODEL AND STUDY PARTICIPANT DETAILS
  - Cell lines
  - Primary culture of mouse embryonic fibroblasts (MEF)
- METHOD DETAILS
  - Constructs
  - cDNA transfection and siRNA knock-down
  - Drugs
  - Antibodies
  - Immunofluorescence, time-lapse imaging, and integrated fluorescence analysis
  - Proximity ligation assay (PLA)
  - Electronic microscopy
  - Immunoblot assays and subcellular fractionation
  - FACS and mitochondrial probes
  - Ca^{2+} measurement
  - Measure of oxygen consumption rate (OCR)
  - Analysis of total ATP levels
- QUANTIFICATION AND STATISTICAL ANALYSIS

SUPPLEMENTAL INFORMATION

Supplemental information can be found online at https://doi.org/10.1016/j.isci.2024.110683.

ACKNOWLEDGMENTS

This study was supported by Genethon (Evry, France), University of Paris-Saclay, and the nonprofit association APSHE (Aide à la recherche médicale contre la Paraplégie Spastique Héréditaire et Nos Enfants). A.R. was supported by the French ministry of higher education and research. P.P. is supported by Progetti di Rilevante Interesse Nazionale (PRIN2017E5L5P3 and PRIN2020RRJP5L_003). P.P. is grateful to C. degli Scrovegni for her continuous support. S.M. is supported by the Italian Ministry of Health (GR-2019-12369646) and local funds from the University of Ferrara. A.B., A.B.B., A.R., L.V., and M.M. are Genopole's members, first French bio-cluster dedicated to genetics, biotechnologies and biotherapies. We are grateful to the "Imaging and Cytometry Core Facility" of Genethon for technical support and Ile-de-France Region, Conseil Départemental de l'Essonne, Inserm, and GIP Genopole, Evry for the purchase of the equipment.

AUTHOR CONTRIBUTIONS

A.R. performed and analyzed PLA experiments, did Spg4-KO genotyping, and realized and maintained MEF culture. S.M. performed and analyzed Ca^{2+} and subcellular fractionation experiments and wrote some sections of the manuscript. D.L. performed TEM experiments. P.S. performed and analyzed FACS experiments. J.P., R.S., and M.L. performed and analyzed Seahorse experiments. N.B. performed and analyzed total ATP measurements. L.V. performed and analyzed some PLA experiments. A.B. performed and analyzed all others experiments, interpreted the results, and was the major contributor in writing the manuscript. M.M., P.P., and A.B.B. participated to the writing and the critical reading of the manuscript. All authors read and approved the submitted version.

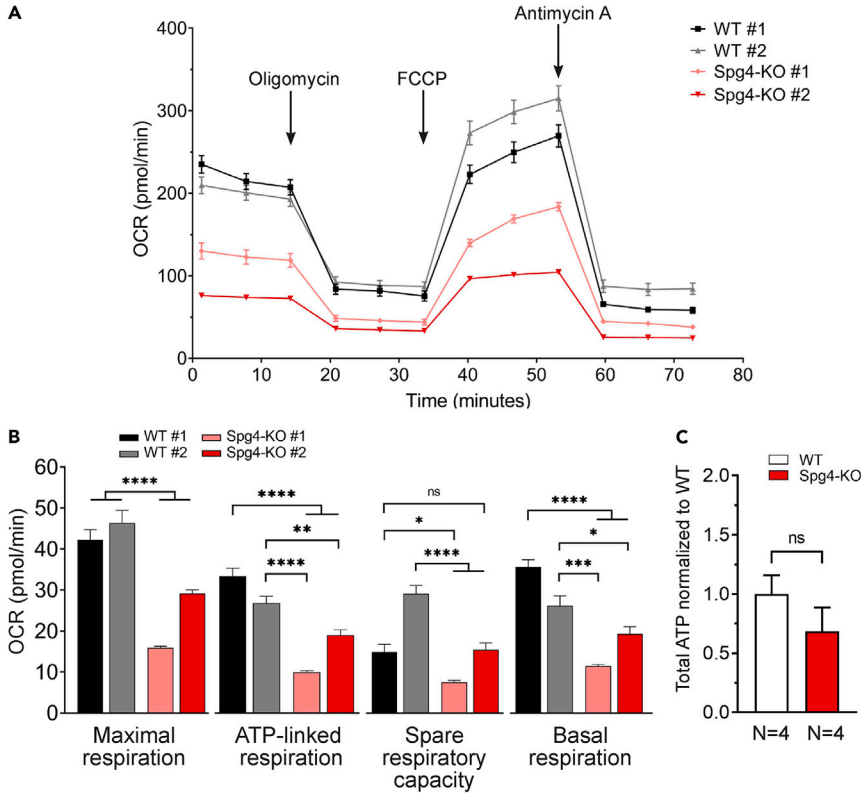

Figure 8. OXPHOS is altered in Spg4-KO MEF

(A) Representative graph of mitochondrial respiration quantified by mitochondrial stress tests performed in WT and Spg4-KO MEF obtained from two different WT and Spg4-KO embryos, respectively.

(B) Comparison of different bioenergetic parameters between WT and Spg4-KO MEF. Data were obtained from at least 20 replicates for each biological sample.

(C) Total ATP levels were measured in protein extracts from four different WT and Spg4-KO MEF lines. Each sample has been analyzed in technical triplicate and the experiments repeated at least two times. Data are normalized to the total ATP levels measured in WT samples. N, number of MEF lines analyzed. Data are shown as mean ± SEM. One-way ANOVA Sidak's multiple comparisons test for (B) and unpaired Student's t test for (C). *$p < 0.05$; **$p < 0.01$; ***$p < 0.005$; ****$p < 0.001$; ns, not significant.

DECLARATION OF INTERESTS

The authors declare no competing interests.

Received: October 10, 2023
Revised: May 20, 2024
Accepted: August 5, 2024
Published: August 6, 2024

REFERENCES

1. Roll-Mecak, A., and Vale, R.D. (2008). Structural basis of microtubule severing by the hereditary spastic paraplegia protein spastin. Nature *451*, 363–367. https://doi.org/10.1038/nature06482.
2. Kuo, Y.W., and Howard, J. (2021). Cutting, Amplifying, and Aligning Microtubules with Severing Enzymes. Trends Cell Biol. *31*, 50–61. https://doi.org/10.1016/j.tcb.2020.10.004.
3. Lo Giudice, T., Lombardi, F., Santorelli, F.M., Kawarai, T., and Orlacchio, A. (2014). Hereditary spastic paraplegia: clinical-genetic characteristics and evolving molecular mechanisms. Exp. Neurol. *261*, 518–539. https://doi.org/10.1016/j.expneurol.2014.06.011.
4. Mohan, N., Qiang, L., Morfini, G., and Baas, P.W. (2021). Therapeutic Strategies for Mutant SPAST-Based Hereditary Spastic Paraplegia. Brain Sci. *11*, 1081. https://doi.org/10.3390/brainsci11081081.
5. Fink, J.K. (2013). Hereditary spastic paraplegia: clinico-pathologic features and emerging molecular mechanisms. Acta Neuropathol. *126*, 307–328. https://doi.org/10.1007/s00401-013-1115-8.
6. Claudiani, P., Riano, E., Errico, A., Andolfi, G., and Rugarli, E.I. (2005). Spastin subcellular localization is regulated through usage of different translation start sites and active export from the nucleus. Exp. Cell Res. *309*, 358–369.
7. Park, S.H., Zhu, P.P., Parker, R.L., and Blackstone, C. (2010). Hereditary spastic paraplegia proteins REEP1, spastin, and atlastin-1 coordinate microtubule interactions with the tubular ER network. J. Clin. Invest. *120*, 1097–1110. https://doi.org/10.1172/JCI40979.
8. Sanderson, C.M., Connell, J.W., Edwards, T.L., Bright, N.A., Duley, S., Thompson, A., Luzio, J.P., and Reid, E. (2006). Spastin and atlastin, two proteins mutated in autosomal-dominant hereditary spastic paraplegia, are

binding partners. Hum. Mol. Genet. *15*, 307–318. https://doi.org/10.1093/hmg/ddi447.

9. Evans, K., Keller, C., Pavur, K., Glasgow, K., Conn, B., and Lauring, B. (2006). Interaction of two hereditary spastic paraplegia gene products, spastin and atlastin, suggests a common pathway for axonal maintenance. Proc. Natl. Acad. Sci. USA *103*, 10666–10671. https://doi.org/10.1073/pnas.0510863103.
10. Mannan, A.U., Boehm, J., Sauter, S.M., Rauber, A., Byrne, P.C., Neesen, J., and Engel, W. (2006). Spastin, the most commonly mutated protein in hereditary spastic paraplegia interacts with Reticulon 1 an endoplasmic reticulum protein. Neurogenetics *7*, 93–103. https://doi.org/10.1007/s10048-006-0034-4.
11. Montenegro, G., Rebelo, A.P., Connell, J., Allison, R., Babalini, C., D'Aloia, M., Montieri, P., Schüle, R., Ishiura, H., Price, J., et al. (2012). Mutations in the ER-shaping protein reticulon 2 cause the axon-degenerative disorder hereditary spastic paraplegia type 12. J. Clin. Invest. *122*, 538–544. https://doi.org/10.1172/JCI60560.
12. Goyal, U., and Blackstone, C. (2013). Untangling the web: mechanisms underlying ER network formation. Biochim. Biophys. Acta *1833*, 2492–2498. https://doi.org/10.1016/j.bbamcr.2013.04.009.
13. McMahon, H.T., and Boucrot, E. (2015). Membrane curvature at a glance. J. Cell Sci. *128*, 1065–1070. https://doi.org/10.1242/jcs.114454.
14. Blackstone, C., O'Kane, C.J., and Reid, E. (2011). Hereditary spastic paraplegias: membrane traffic and the motor pathway. Nature reviews *12*, 31–42. https://doi.org/10.1038/nrn2946.
15. Sonda, S., Pendin, D., and Daga, A. (2021). ER Morphology in the Pathogenesis of Hereditary Spastic Paraplegia. Cells *10*, 2870. https://doi.org/10.3390/cells10112870.
16. Plaud, C., Joshi, V., Kajevu, N., Pous, C., Curmi, P.A., and Burgo, A. (2018). Functional differences of short and long isoforms of spastin harboring missense mutation. Disease Models & Mechanisms *11*, dmm033704. https://doi.org/10.1242/dmm.033704.
17. Rizo, T., Gebhardt, L., Riedlberger, J., Eberhardt, E., Fester, L., Alansary, D., Winkler, J., Turan, S., Arnold, P., Niemeyer, B.A., et al. (2022). Store-operated calcium entry is reduced in spastin-linked hereditary spastic paraplegia. Brain *145*, 3131–3146. https://doi.org/10.1093/brain/awac122.
18. Arribat, Y., Grepper, D., Lagarrigue, S., Qi, T., Cohen, S., and Amati, F. (2020). Spastin mutations impair coordination between lipid droplet dispersion and reticulum. PLoS Genet. *16*, e1008665. https://doi.org/10.1371/journal.pgen.1008665.
19. Vajente, N., Norante, R., Redolfi, N., Daga, A., Pizzo, P., and Pendin, D. (2019). Microtubules Stabilization by Mutant Spastin Affects ER Morphology and Ca(2+) Handling. Front. Physiol. *10*, 1544. https://doi.org/10.3389/fphys.2019.01544.
20. Wu, H., Carvalho, P., and Voeltz, G.K. (2018). Here, there, and everywhere: The importance of ER membrane contact sites. Science *361*, eaan5835. https://doi.org/10.1126/science.aan5835.
21. Phillips, M.J., and Voeltz, G.K. (2016). Structure and function of ER membrane contact sites with other organelles. Nat. Rev. Mol. Cell Biol. *17*, 69–82. https://doi.org/10.1038/nrm.2015.8.
22. Giacomello, M., and Pellegrini, L. (2016). The coming of age of the mitochondria-ER contact: a matter of thickness. Cell Death Differ. *23*, 1417–1427. https://doi.org/10.1038/cdd.2016.52.
23. Missiroli, S., Perrone, M., Gafà, R., Nicoli, F., Bonora, M., Morciano, G., Boncompagni, C., Marchi, S., Lebiedzinska-Arciszewska, M., Vezzani, B., et al. (2023). PML at mitochondria-associated membranes governs a trimeric complex with NLRP3 and P2X7R that modulates the tumor immune microenvironment. Cell Death Differ. *30*, 429–441. https://doi.org/10.1038/s41418-022-01095-9.
24. Giorgi, C., Marchi, S., and Pinton, P. (2018). The machineries, regulation and cellular functions of mitochondrial calcium. Nat. Rev. Mol. Cell Biol. *19*, 713–730. https://doi.org/10.1038/s41580-018-0052-8.
25. Wang, X., Xing, C., Li, G., Dai, X., Gao, X., Zhuang, Y., Cao, H., Hu, G., Guo, X., and Yang, F. (2023). The key role of proteostasis at mitochondria-associated endoplasmic reticulum membrane in vanadium-induced nephrotoxicity using a proteomic strategy. Sci. Total Environ. *869*, 161741. https://doi.org/10.1016/j.scitotenv.2023.161741.
26. Ilacqua, N., Sánchez-Álvarez, M., Bachmann, M., Costiniti, V., Del Pozo, M.A., and Giacomello, M. (2017). Protein Localization at Mitochondria-ER Contact Sites in Basal and Stress Conditions. Front. Cell Dev. Biol. *5*, 107. https://doi.org/10.3389/fcell.2017.00107.
27. Paillusson, S., Stoica, R., Gomez-Suaga, P., Lau, D.H.W., Mueller, S., Miller, T., and Miller, C.C.J. (2016). There's Something Wrong with my MAM; the ER-Mitochondria Axis and Neurodegenerative Diseases. Trends Neurosci. *39*, 146–157. https://doi.org/10.1016/j.tins.2016.01.008.
28. Fowler, P.C., Garcia-Pardo, M.E., Simpson, J.C., and O'Sullivan, N.C. (2019). NeurodegenERation: The Central Role for ER Contacts in Neuronal Function and Axonopathy, Lessons From Hereditary Spastic Paraplegias and Related Diseases. Front. Neurosci. *13*, 1051. https://doi.org/10.3389/fnins.2019.01051.
29. Plaud, C., Joshi, V., Marinello, M., Pastré, D., Galli, T., Curmi, P.A., and Burgo, A. (2017). Spastin regulates VAMP7-containing vesicles trafficking in cortical neurons. Biochim. Biophys. Acta *1863*, 1666–1677. https://doi.org/10.1016/j.bbadis.2017.04.007.
30. Havlicek, S., Kohl, Z., Mishra, H.K., Prots, I., Eberhardt, E., Denguir, N., Wend, H., Plötz, S., Boyer, L., Marchetto, M.C.N., et al. (2014). Gene dosage-dependent rescue of HSP neurite defects in SPG4 patients' neurons. Hum. Mol. Genet. *23*, 2527–2541. https://doi.org/10.1093/hmg/ddt644.
31. Kasher, P.R., De Vos, K.J., Wharton, S.B., Manser, C., Bennett, E.J., Bingley, M., Wood, J.D., Milner, R., McDermott, C.J., Miller, C.C.J., et al. (2009). Direct evidence for axonal transport defects in a novel mouse model of mutant spastin-induced hereditary spastic paraplegia (HSP) and human HSP patients. J. Neurochem. *110*, 34–44.
32. Denton, K.R., Lei, L., Grenier, J., Rodionov, V., Blackstone, C., and Li, X.J. (2014). Loss of spastin function results in disease-specific axonal defects in human pluripotent stem cell-based models of hereditary spastic paraplegia. Stem Cell. *32*, 414–423. https://doi.org/10.1002/stem.1569.
33. Wali, G., Berkovsky, S., Whiten, D.R., Mackay-Sim, A., and Sue, C.M. (2021). Single cell morphology distinguishes genotype and drug effect in Hereditary Spastic Paraplegia. Sci. Rep. *11*, 16635. https://doi.org/10.1038/s41598-021-95995-4.
34. Dong, E.L., Wang, C., Wu, S., Lu, Y.Q., Lin, X.H., Su, H.Z., Zhao, M., He, J., Ma, L.X., Wang, N., et al. (2018). Clinical spectrum and genetic landscape for hereditary spastic paraplegias in China. Mol. Neurodegener. *13*, 36. https://doi.org/10.1186/s13024-018-0269-1.
35. Parodi, L., Barbier, M., Jacoupy, M., Pujol, C., Lejeune, F.X., Lallemant-Dudek, P., Esteves, T., Pennings, M., Kamsteeg, E.J., Guillaud-Bataille, M., et al. (2022). The mitochondrial seryl-tRNA synthetase SARS2 modifies onset in spastic paraplegia type 4. Genet. Med. *24*, 2308–2317. https://doi.org/10.1016/j.gim.2022.07.023.
36. Solowska, J.M., D'Rozario, M., Jean, D.C., Davidson, M.W., Marenda, D.R., and Baas, P.W. (2014). Pathogenic Mutation of Spastin Has Gain-of-Function Effects on Microtubule Dynamics. J. Neurosci. *34*, 1856–1867. https://doi.org/10.1523/JNEUROSCI.3309-13.2014.
37. White, S.R., Evans, K.J., Lary, J., Cole, J.L., and Lauring, B. (2007). Recognition of C-terminal amino acids in tubulin by pore loops in Spastin is important for microtubule severing. J. Cell Biol. *176*, 995–1005. https://doi.org/10.1083/jcb.200610072.
38. Wieckowski, M.R., Giorgi, C., Lebiedzinska, M., Duszynski, J., and Pinton, P. (2009). Isolation of mitochondria-associated membranes and mitochondria from animal tissues and cells. Nat. Protoc. *4*, 1582–1590. https://doi.org/10.1038/nprot.2009.151.
39. Bernard-Marissal, N., Chrast, R., and Schneider, B.L. (2018). Endoplasmic reticulum and mitochondria in diseases of motor and sensory neurons: a broken relationship? Cell Death Dis. *9*, 333. https://doi.org/10.1038/s41419-017-0125-1.
40. Hegazy, M., Cohen-Barak, E., Koetsier, J.L., Najor, N.A., Arvanitis, C., Sprecher, E., Green, K.J., and Godsel, L.M. (2020). Proximity Ligation Assay for Detecting Protein-Protein Interactions and Protein Modifications in Cells and Tissues in Situ. Curr. Protoc. Cell Biol. *89*, e115. https://doi.org/10.1002/cpcb.115.
41. Tubbs, E., and Rieusset, J. (2016). Study of Endoplasmic Reticulum and Mitochondria Interactions by In Situ Proximity Ligation Assay in Fixed Cells. J. Vis. Exp. e54899. https://doi.org/10.3791/54899.
42. Benhammouda, S., Vishwakarma, A., Gatti, P., and Germain, M. (2021). Mitochondria Endoplasmic Reticulum Contact Sites (MERCs): Proximity Ligation Assay as a Tool to Study Organelle Interaction. Front. Cell Dev. Biol. *9*, 789959. https://doi.org/10.3389/fcell.2021.789959.
43. Xicoy, H., Wieringa, B., and Martens, G.J.M. (2017). The SH-SY5Y cell line in Parkinson's disease research: a systematic review. Mol. Neurodegener. *12*, 10. https://doi.org/10.1186/s13024-017-0149-0.
44. Simoes, R.F., Ferrao, R., Silva, M.R., Pinho, S.L.C., Ferreira, L., Oliveira, P.J., and Cunha-Oliveira, T. (2021). Refinement of a differentiation protocol using

neuroblastoma SH-SY5Y cells for use in neurotoxicology research. Food Chem. Toxicol. *149*, 111967. https://doi.org/10.1016/j.fct.2021.111967.

45. Kelle, D., Kırımtay, K., Selçuk, E., and Karabay, A. (2019). Elk1 affects katanin and spastin proteins via differential transcriptional and post-transcriptional regulations. PLoS One *14*, e0212518. https://doi.org/10.1371/journal.pone.0212518.
46. Lim, J.H., Kang, H.M., Jung, H.R., Kim, D.S., Noh, K.H., Chang, T.K., Kim, B.J., Sung, D.H., Cho, H.S., Chung, K.S., et al. (2018). Missense mutation of SPAST protein (I344K) results in loss of ATPase activity and prolonged the half-life, implicated in autosomal dominant hereditary spastic paraplegia. Biochim. Biophys. Acta, Mol. Basis Dis. *1864*, 3221–3233. https://doi.org/10.1016/j.bbadis.2018.07.009.
47. Leo, L., Weissmann, C., Burns, M., Kang, M., Song, Y., Qiang, L., Brady, S.T., Baas, P.W., and Morfini, G. (2017). Mutant spastin proteins promote deficits in axonal transport through an isoform-specific mechanism involving casein kinase 2 activation. Hum. Mol. Genet. *26*, 2321–2334. https://doi.org/10.1093/hmg/ddx125.
48. Gurel, P.S., Hatch, A.L., and Higgs, H.N. (2014). Connecting the cytoskeleton to the endoplasmic reticulum and Golgi. Curr. Biol. *24*, R660–R672. https://doi.org/10.1016/j.cub.2014.05.033.
49. Perkins, H.T., and Allan, V. (2021). Intertwined and Finely Balanced: Endoplasmic Reticulum Morphology, Dynamics, Function, and Diseases. Cells *10*, 2341. https://doi.org/10.3390/cells10092341.
50. Waterman-Storer, C.M., and Salmon, E.D. (1998). Endoplasmic reticulum membrane tubules are distributed by microtubules in living cells using three distinct mechanisms. Curr. Biol. *8*, 798–806. https://doi.org/10.1016/s0960-9822(98)70321-5.
51. Friedman, J.R., Webster, B.M., Mastronarde, D.N., Verhey, K.J., and Voeltz, G.K. (2010). ER sliding dynamics and ER-mitochondrial contacts occur on acetylated microtubules. J. Cell Biol. *190*, 363–375. https://doi.org/10.1083/jcb.200911024.
52. Janke, C., and Montagnac, G. (2017). Causes and Consequences of Microtubule Acetylation. Curr. Biol. *27*, R1287–R1292. https://doi.org/10.1016/j.cub.2017.10.044.
53. Orso, G., Martinuzzi, A., Rossetto, M.G., Sartori, E., Feany, M., and Daga, A. (2005). Disease-related phenotypes in a Drosophila model of hereditary spastic paraplegia are ameliorated by treatment with vinblastine. J. Clin. Invest. *115*, 3026–3034. https://doi.org/10.1172/JCI24694.
54. Janke, C., and Magiera, M.M. (2020). The tubulin code and its role in controlling microtubule properties and functions. Nat. Rev. Mol. Cell Biol. *21*, 307–326. https://doi.org/10.1038/s41580-020-0214-3.
55. Connell, J.W., Allison, R.J., Rodger, C.E., Pearson, G., Zlamalova, E., and Reid, E. (2020). ESCRT-III-associated proteins and spastin inhibit protrudin-dependent polarised membrane traffic. Cell. Mol. Life Sci. *77*, 2641–2658. https://doi.org/10.1007/s00018-019-03313-z.
56. Hazan, J., Fonknechten, N., Mavel, D., Paternotte, C., Samson, D., Artiguenave, F., Davoine, C.S., Cruaud, C., Dürr, A., Wincker, P., et al. (1999). Spastin, a new AAA protein, is altered in the most frequent form of autosomal dominant spastic paraplegia. Nat. Genet. *23*, 296–303. https://doi.org/10.1038/15472.
57. Wai, T., and Langer, T. (2016). Mitochondrial Dynamics and Metabolic Regulation. Trends Endocrinol. Metabol. *27*, 105–117. https://doi.org/10.1016/j.tem.2015.12.001.
58. Tabara, L.C., Morris, J.L., and Prudent, J. (2021). The Complex Dance of Organelles during Mitochondrial Division. Trends Cell Biol. *31*, 241–253. https://doi.org/10.1016/j.tcb.2020.12.005.
59. Abrisch, R.G., Gumbin, S.C., Wisniewski, B.T., Lackner, L.L., and Voeltz, G.K. (2020). Fission and fusion machineries converge at ER contact sites to regulate mitochondrial morphology. J. Cell Biol. *219*, e201911122. https://doi.org/10.1083/jcb.201911122.
60. Friedman, J.R., Lackner, L.L., West, M., DiBenedetto, J.R., Nunnari, J., and Voeltz, G.K. (2011). ER tubules mark sites of mitochondrial division. Science *334*, 358–362. https://doi.org/10.1126/science.1207385.
61. Guo, Y., Li, D., Zhang, S., Yang, Y., Liu, J.J., Wang, X., Liu, C., Milkie, D.E., Moore, R.P., Tulu, U.S., et al. (2018). Visualizing Intracellular Organelle and Cytoskeletal Interactions at Nanoscale Resolution on Millisecond Timescales. Cell *175*, 1430–1442.e17. https://doi.org/10.1016/j.cell.2018.09.057.
62. Miyazono, Y., Hirashima, S., Ishihara, N., Kusukawa, J., Nakamura, K.I., and Ohta, K. (2018). Uncoupled mitochondria quickly shorten along their long axis to form indented spheroids, instead of rings, in a fission-independent manner. Sci. Rep. *8*, 350. https://doi.org/10.1038/s41598-017-18582-6.
63. Zhou, R., Yazdi, A.S., Menu, P., and Tschopp, J. (2011). A role for mitochondria in NLRP3 inflammasome activation. Nature *469*, 221–225. https://doi.org/10.1038/nature09663.
64. Ji, W.K., Chakrabarti, R., Fan, X., Schoenfeld, L., Strack, S., and Higgs, H.N. (2017). Receptor-mediated Drp1 oligomerization on endoplasmic reticulum. J. Cell Biol. *216*, 4123–4139. https://doi.org/10.1083/jcb.201610057.
65. Bonora, M., Giorgi, C., and Pinton, P. (2022). Molecular mechanisms and consequences of mitochondrial permeability transition. Nat. Rev. Mol. Cell Biol. *23*, 266–285. https://doi.org/10.1038/s41580-021-00433-y.
66. Romero-Garcia, S., and Prado-Garcia, H. (2019). Mitochondrial calcium: Transport and modulation of cellular processes in homeostasis and cancer (Review). Int. J. Oncol. *54*, 1155–1167. https://doi.org/10.3892/ijo.2019.4696.
67. Fink, B.D., Bai, F., Yu, L., and Sivitz, W.I. (2017). Regulation of ATP production: dependence on calcium concentration and respiratory state. Am. J. Physiol. Cell Physiol. *313*, C146–C153. https://doi.org/10.1152/ajpcell.00086.2017.
68. Giorgi, C., Missiroli, S., Patergnani, S., Duszynski, J., Wieckowski, M.R., and Pinton, P. (2015). Mitochondria-associated membranes: composition, molecular mechanisms, and physiopathological implications. Antioxidants Redox Signal. *22*, 995–1019. https://doi.org/10.1089/ars.2014.6223.
69. Sano, R., Annunziata, I., Patterson, A., Moshiach, S., Gomero, E., Opferman, J., Forte, M., and d'Azzo, A. (2009). GM1-ganglioside accumulation at the mitochondria-associated ER membranes links ER stress to Ca(2+)-dependent mitochondrial apoptosis. Mol. Cell *36*, 500–511. https://doi.org/10.1016/j.molcel.2009.10.021.
70. Cherubini, M., Lopez-Molina, L., and Gines, S. (2020). Mitochondrial fission in Huntington's disease mouse striatum disrupts ER-mitochondria contacts leading to disturbances in Ca(2+) efflux and Reactive Oxygen Species (ROS) homeostasis. Neurobiol. Dis. *136*, 104741. https://doi.org/10.1016/j.nbd.2020.104741.
71. Bonora, M., Giorgi, C., Bononi, A., Marchi, S., Patergnani, S., Rimessi, A., Rizzuto, R., and Pinton, P. (2013). Subcellular calcium measurements in mammalian cells using jellyfish photoprotein aequorin-based probes. Nat. Protoc. *8*, 2105–2118. https://doi.org/10.1038/nprot.2013.127.
72. Yoboue, E.D., Sitia, R., and Simmen, T. (2018). Redox crosstalk at endoplasmic reticulum (ER) membrane contact sites (MCS) uses toxic waste to deliver messages. Cell Death Dis. *9*, 331. https://doi.org/10.1038/s41419-017-0033-4.
73. Fan, Y., and Simmen, T. (2019). Mechanistic Connections between Endoplasmic Reticulum (ER) Redox Control and Mitochondrial Metabolism. Cells *8*, 1071. https://doi.org/10.3390/cells8091071.
74. Perrone, M., Caroccia, N., Genovese, I., Missiroli, S., Modesti, L., Pedriali, G., Vezzani, B., Vitto, V.A.M., Antenori, M., Lebiedzinska-Arciszewska, M., et al. (2020). The role of mitochondria-associated membranes in cellular homeostasis and diseases. Int. Rev. Cell Mol. Biol. *350*, 119–196. https://doi.org/10.1016/bs.ircmb.2019.11.002.
75. McCormack, J.G., Halestrap, A.P., and Denton, R.M. (1990). Role of calcium ions in regulation of mammalian intramitochondrial metabolism. Physiol. Rev. *70*, 391–425. https://doi.org/10.1152/physrev.1990.70.2.391.
76. Wang, J.Q., Chen, Q., Wang, X., Wang, Q.C., Wang, Y., Cheng, H.P., Guo, C., Sun, Q., Chen, Q., and Tang, T.S. (2013). Dysregulation of mitochondrial calcium signaling and superoxide flashes cause mitochondrial genomic DNA damage in Huntington disease. J. Biol. Chem. *288*, 3070–3084. https://doi.org/10.1074/jbc.M112.407726.
77. Dikalov, S.I., and Harrison, D.G. (2014). Methods for detection of mitochondrial and cellular reactive oxygen species. Antioxidants Redox Signal. *20*, 372–382. https://doi.org/10.1089/ars.2012.4886.
78. Korshunov, S.S., Skulachev, V.P., and Starkov, A.A. (1997). High protonic potential actuates a mechanism of production of reactive oxygen species in mitochondria. FEBS Lett. *416*, 15–18. https://doi.org/10.1016/s0014-5793(97)01159-9.
79. Suski, J.M., Lebiedzinska, M., Bonora, M., Pinton, P., Duszynski, J., and Wieckowski, M.R. (2012). Relation between mitochondrial membrane potential and ROS formation. Methods Mol. Biol. *810*, 183–205. https://doi.org/10.1007/978-1-61779-382-0_12.
80. Brand, M.D., Affourtit, C., Esteves, T.C., Green, K., Lambert, A.J., Miwa, S., Pakay, J.L., and Parker, N. (2004). Mitochondrial superoxide: production, biological effects, and activation of uncoupling proteins. Free

Radic. Biol. Med. *37*, 755–767. https://doi.org/10.1016/j.freeradbiomed.2004.05.034.

81. Xiong, J., Camello, P.J., Verkhratsky, A., and Toescu, E.C. (2004). Mitochondrial polarisation status and [Ca2+]i signalling in rat cerebellar granule neurones aged in vitro. Neurobiol. Aging *25*, 349–359. https://doi.org/10.1016/S0197-4580(03)00123-4.
82. Scaduto, R.C., Jr., and Grotyohann, L.W. (1999). Measurement of mitochondrial membrane potential using fluorescent rhodamine derivatives. Biophys. J. *76*, 469–477. https://doi.org/10.1016/S0006-3495(99)77214-0.
83. Brand, M.D., and Nicholls, D.G. (2011). Assessing mitochondrial dysfunction in cells. Biochem. J. *435*, 297–312. https://doi.org/10.1042/BJ20110162.
84. Yepez, V.A., Kremer, L.S., Iuso, A., Gusic, M., Kopajtich, R., Konarikova, E., Nadel, A., Wachutka, L., Prokisch, H., and Gagneur, J. (2018). OCR-Stats: Robust estimation and statistical testing of mitochondrial respiration activities using Seahorse XF Analyzer. PLoS One *13*, e0199938. https://doi.org/10.1371/journal.pone.0199938.
85. Solowska, J.M., Garbern, J.Y., and Baas, P.W. (2010). Evaluation of loss of function as an explanation for SPG4-based hereditary spastic paraplegia. Hum. Mol. Genet. *19*, 2767–2779. https://doi.org/10.1093/hmg/ddq177.
86. Lewis, R.S. (2007). The molecular choreography of a store-operated calcium channel. Nature *446*, 284–287. https://doi.org/10.1038/nature05637.
87. Wali, G., Kumar, K.R., Liyanage, E., Davis, R.L., Mackay-Sim, A., and Sue, C.M. (2020). Mitochondrial Function in Hereditary Spastic Paraplegia: Deficits in SPG7 but Not SPAST Patient-Derived Stem Cells. Front. Neurosci. *14*, 820. https://doi.org/10.3389/fnins.2020.00820.
88. Chang, C.L., Weigel, A.V., Ioannou, M.S., Pasolli, H.A., Xu, C.S., Peale, D.R., Shtengel, G., Freeman, M., Hess, H.F., Blackstone, C., and Lippincott-Schwartz, J. (2019). Spastin tethers lipid droplets to peroxisomes and directs fatty acid trafficking through ESCRT-III. J. Cell Biol. *218*, 2583–2599. https://doi.org/10.1083/jcb.201902061.
89. Papadopoulos, C., Orso, G., Mancuso, G., Herholz, M., Gumeni, S., Tadepalle, N., Jüngst, C., Tzschichholz, A., Schauss, A., Höning, S., et al. (2015). Spastin binds to lipid droplets and affects lipid metabolism. PLoS Genet. *11*, e1005149. https://doi.org/10.1371/journal.pgen.1005149.
90. Schuldiner, M., and Bohnert, M. (2017). A different kind of love - lipid droplet contact sites. Biochim. Biophys. Acta Mol. Cell Biol. Lipids *1862*, 1188–1196. https://doi.org/10.1016/j.bbalip.2017.06.005.
91. Thiam, A.R., and Ikonen, E. (2021). Lipid Droplet Nucleation. Trends Cell Biol. *31*, 108–118. https://doi.org/10.1016/j.tcb.2020.11.006.
92. Tadepalle, N., Robers, L., Veronese, M., Zentis, P., Babatz, F., Brodesser, S., Gruszczyk, A.V., Schauss, A., Höning, S., and Rugarli, E.I. (2020). Microtubule-dependent and independent roles of spastin in lipid droplet dispersion and biogenesis. Life Sci. Alliance *3*, e202000715. https://doi.org/10.26508/lsa.202000715.
93. Guyard, V., Monteiro-Cardoso, V.F., Omrane, M., Sauvanet, C., Houcine, A., Boulogne, C., Ben Mbarek, K., Vitale, N., Faklaris, O., El Khallouki, N., et al. (2022). ORP5 and ORP8 orchestrate lipid droplet biogenesis and maintenance at ER-mitochondria contact sites. J. Cell Biol. *221*, e202112107. https://doi.org/10.1083/jcb.202112107.
94. Denton, R.M. (2009). Regulation of mitochondrial dehydrogenases by calcium ions. Biochim. Biophys. Acta *1787*, 1309–1316. https://doi.org/10.1016/j.bbabio.2009.01.005.
95. Csordas, G., Renken, C., Varnai, P., Walter, L., Weaver, D., Buttle, K.F., Balla, T., Mannella, C.A., and Hajnoczky, G. (2006). Structural and functional features and significance of the physical linkage between ER and mitochondria. J. Cell Biol. *174*, 915–921. https://doi.org/10.1083/jcb.200604016.
96. Hedskog, L., Pinho, C.M., Filadi, R., Rönnbäck, A., Hertwig, L., Wiehager, B., Larssen, P., Gellhaar, S., Sandebring, A., Westerlund, M., et al. (2013). Modulation of the endoplasmic reticulum-mitochondria interface in Alzheimer's disease and related models. Proc. Natl. Acad. Sci. USA *110*, 7916–7921. https://doi.org/10.1073/pnas.1300677110.
97. NavaneethaKrishnan, S., Rosales, J.L., and Lee, K.Y. (2020). mPTP opening caused by Cdk5 loss is due to increased mitochondrial Ca(2+) uptake. Oncogene *39*, 2797–2806. https://doi.org/10.1038/s41388-020-1188-5.
98. Thoudam, T., Ha, C.M., Leem, J., Chanda, D., Park, J.S., Kim, H.J., Jeon, J.H., Choi, Y.K., Liangpunsakul, S., Huh, Y.H., et al. (2019). PDK4 Augments ER-Mitochondria Contact to Dampen Skeletal Muscle Insulin Signaling During Obesity. Diabetes *68*, 571–586. https://doi.org/10.2337/db18-0363.
99. Arruda, A.P., Pers, B.M., Parlakgül, G., Güney, E., Inouye, K., and Hotamisligil, G.S. (2014). Chronic enrichment of hepatic endoplasmic reticulum-mitochondria contact leads to mitochondrial dysfunction in obesity. Nat. Med. *20*, 1427–1435. https://doi.org/10.1038/nm.3735.
100. Long, Q., Zhao, D., Fan, W., Yang, L., Zhou, Y., Qi, J., Wang, X., and Liu, X. (2015). Modeling of Mitochondrial Donut Formation. Biophys. J. *109*, 892–899. https://doi.org/10.1016/j.bpj.2015.07.039.
101. Zhu, Y., Zhang, G., Lin, S., Shi, J., Zhang, H., and Hu, J. (2018). Sec61beta facilitates the maintenance of endoplasmic reticulum homeostasis by associating microtubules. Protein Cell *9*, 616–628. https://doi.org/10.1007/s13238-017-0492-5.
102. Wang, S., Tukachinsky, H., Romano, F.B., and Rapoport, T.A. (2016). Cooperation of the ER-shaping proteins atlastin, lunapark, and reticulons to generate a tubular membrane network. Elife *5*, e18605. https://doi.org/10.7554/eLife.18605.
103. Liu, X., Guo, X., Niu, L., Li, X., Sun, F., Hu, J., Wang, X., and Shen, K. (2019). Atlastin-1 regulates morphology and function of endoplasmic reticulum in dendrites. Nat. Commun. *10*, 568. https://doi.org/10.1038/s41467-019-08478-6.
104. Renvoise, B., Malone, B., Falgairolle, M., Munasinghe, J., Stadler, J., Sibilla, C., Park, S.H., and Blackstone, C. (2016). Reep1 null mice reveal a converging role for hereditary spastic paraplegia proteins in lipid droplet regulation. Hum. Mol. Genet. *25*, 5111–5125. https://doi.org/10.1093/hmg/ddw315.
105. Tarrade, A., Fassier, C., Courageot, S., Charvin, D., Vitte, J., Peris, L., Thorel, A., Mouisel, E., Fonknechten, N., Roblot, N., et al. (2006). A mutation of spastin is responsible for swellings and impairment of transport in a region of axon characterized by changes in microtubule composition. Hum. Mol. Genet. *15*, 3544–3558.
106. Fassier, C., Tarrade, A., Peris, L., Courageot, S., Mailly, P., Dalard, C., Delga, S., Roblot, N., Lefèvre, J., Job, D., et al. (2013). Microtubule-targeting drugs rescue axonal swellings in cortical neurons from spastin knockout mice. Dis. Model. Mech. *6*, 72–83. https://doi.org/10.1242/dmm.008946.
107. Jozefczuk, J., Drews, K., and Adjaye, J. (2012). Preparation of mouse embryonic fibroblast cells suitable for culturing human embryonic and induced pluripotent stem cells. J. Vis. Exp. 3854. https://doi.org/10.3791/3854.
108. Reynolds, E.S. (1963). The use of lead citrate at high pH as an electron-opaque stain in electron microscopy. J. Cell Biol. *17*, 208–212. https://doi.org/10.1083/jcb.17.1.208.
109. Vance, J.E. (1990). Phospholipid synthesis in a membrane fraction associated with mitochondria. J. Biol. Chem. *265*, 7248–7256.
110. Correia-Melo, C., Marques, F.D.M., Anderson, R., Hewitt, G., Hewitt, R., Cole, J., Carroll, B.M., Miwa, S., Birch, J., Merz, A., et al. (2016). Mitochondria are required for pro-ageing features of the senescent phenotype. EMBO J. *35*, 724–742. https://doi.org/10.15252/embj.201592862.
111. Perez, M.J., Ponce, D.P., Osorio-Fuentealba, C., Behrens, M.I., and Quintanilla, R.A. (2017). Mitochondrial Bioenergetics Is Altered in Fibroblasts from Patients with Sporadic Alzheimer's Disease. Front. Neurosci. *11*, 553. https://doi.org/10.3389/fnins.2017.00553.

STAR★METHODS

KEY RESOURCES TABLE

REAGENT or RESOURCE	SOURCE	IDENTIFIER
Antibodies		
Acetylated tubulin clone 6-11B-1 (mouse monoclonal)	Sigma-Aldrich	Cat# MABT868; RRID: AB_2819178
Beta3-tubulin (rabbit monoclonal)	Cell signaling	Cat# 5568; RRID: AB_10694505
Beta-tubulin (rabbit polyclonal)	Abcam	Cat# ab6046; RRID: AB_2210370
Calreticulin (rabbit polyclonal)	Thermoscientific	Cat# PA3-900; RRID: AB_325990
Cytochrome *c* (mouse monoclonal)	BD Biosciences	Cat# 556433; RRID: AB_396417
DRP1 (rabbit polyclonal)	Proteintech	Cat# 12957-1-AP; RRID: AB_2093525
DRP1-Phospho ser616 (rabbit polyclonal)	Cell signaling	Cat# 4494; RRID: AB_11178659
Flag clone M2 (mouse monoclonal)	Sigma-Aldrich	Cat# F1804; RRID: AB_262044
GAPDH 71.1 (mouse monoclonal)	Sigma-Aldrich	Cat# G8795; RRID: AB_1078991
IP3R3 (mouse monoclonal)	BD Biosciences	Cat# 610312; RRID: AB_397704
IP3R (rabbit polyclonal)	Abcam	Cat# ab5804; RRID: AB_305124
MCU/CCDC109A (rabbit polyclonal)	Proteintech	Cat# 26312-1; RRID: AB_2880474
SigmaR1 (rabbit polyclonal)	Sigma-Aldrich	Cat# HPA018002; RRID: AB_1854802
SigmaR1 (rabbit polyclonal)	Proteintech	Cat# 15168-1-AP; RRID: AB_2301712
Spastin 6C6 (mouse monoclonal)	Abcam	Cat# ab77144; RRID: AB_1524436
TOM20 (mouse monoclonal)	Abcam	Cat# ab56783; RRID: AB_945896
TOM20 (rabbit polyclonal)	Proteintech	Cat# 11802-1-AP; RRID: AB_2207530
TOM40 (rabbit polyclonal)	Proteintech	Cat# 18409-1-AP; RRID: AB_2303725
TOM70 (rabbit polyclonal)	Proteintech	Cat# 14528-1-AP; RRID: AB_2303727
Tyrosinated tubulin clone YL1/2 (rat monoclonal)	Millipore	Cat# MAB1864; RRID: AB_2210391
VDAC1 (rabbit polyclonal)	Abcam	Cat# ab15895; RRID: AB_2214787
VDAC1 (mouse monoclonal)	Abcam	Cat# ab14734; RRID: AB_443084
Alexa Fluor 488 Goat anti-rabbit secondary	Invitrogen	RRID: AB_143165
Alexa Fluor 594 Goat anti-mouse secondary	Invitrogen	RRID: AB_2534073
Alexa Fluor 647 Goat anti-mouse secondary	Invitrogen	RRID: AB_2535804
Alexa Fluor 488 Goat anti-rat secondary	Invitrogen	RRID: AB_2534074
Alexa Fluor 680 Goat anti-mouse secondary	Invitrogen	RRID: AB_2535723
IRDye 800 CW Goat anti-rabbit secondary	LI-COR Bioscience	Cat# 926-32211; RRID: AB_621843
Chemicals, peptides, and recombinant proteins		
Antimycin A	Sigma-Aldrich	Cat# A8674
Oligomycin	Sigma-Aldrich	Cat# 495455
FCCP	Sigma-Aldrich	Cat# C2920
Adenosine 5-triphosphate disodium salt hydrate	Sigma-Aldrich	Cat# A26209
Charbachol	Merck Millipore	Cat# 212385-M
Histamine dihydrochloride	Sigma-Aldrich	Cat# H27250
TMRM	Invitrogen	Cat# I34361
MitoTracker green	Invitrogen	Cat# M7514
Mitosox Red	Invitrogen	Cat# M36008
JC-1	Invitrogen	Cat# T3168

(*Continued on next page*)

Continued

REAGENT or RESOURCE	SOURCE	IDENTIFIER
Critical commercial assays		
Lipofectamine 2000	Invitrogen	Cat# 11668019
DharmaFECT1	Dharmacon	Cat# T-2001
Pierce™ BCA Protein Assay Kit	ThermoFisher	Cat# C10269
Duolink *in situ* red kit	Sigma Aldrich	Cat# DUO92101
ATP Determination Kit	Invitrogen	Cat# A22066
Passive lysis buffer	Promega	Cat# E194A
Experimental models: Cell lines		
Human: HeLa cells	Genethon's DNA and Cell bank	N/A
Human: HEK cells	Genethon's DNA and Cell bank	N/A
Human: SH-SY5Y	Gift of David PASTRE	N/A
Mouse embryonic fibroblasts (MEF)	Spg4-KO mice	N/A
Experimental models: Organisms/strains		
Mouse: Spg4-KO	(Tarrade et al., 2006)[105]	N/A
Oligonucleotides		
Custom siRNA ON-TARGET plus sequence: *SPAST* siRNA1: 5′-GAACUUCAACCUUCUAUAA-3′, siRNA2: 5′-UAUAAGUGCUGCAAGUUUA-3′	Dharmacon	(Connell et al., 2020)[55]
ON-TARGET plus non-targeting siRNAs (scramble)	Dharmacon	D-001810-10-05
Recombinant DNA		
Plasmid: Spastin M1-EGFP	(Plaud et al., 2018)[16]	N/A
Plasmid: Spastin M1-C448Y-EGFP	(Plaud et al., 2018)[16]	N/A
Plasmid: Spastin M1 Δ-EGFP	(Plaud et al., 2018)[16]	N/A
Plasmid: Spastin M1-Flag-MAT-tag2	This paper	N/A
Plasmid: Spastin M1-R496C-EGFP	This paper	N/A
Plasmid: Mito-mCherry	Gift of Christelle TESSON	N/A
Software and algorithms		
ImageJ	NIH	N/A
Metamorph	Roper Scientific	N/A
Graphpad Prism version 9	Graphpad software	N/A

RESOURCE AVAILABILITY

Lead contact

Further information and requests for resources and reagents should be directed to and will be fulfilled by the lead contact, Andrea BURGO (andrea.burgo@univ-evry.fr).

Materials availability

Plasmids generated in this study are available upon request.

Data and code availability

- All data reported in this paper will be shared by the lead contact upon request.
- This paper does not report original code.
- Any additional information required to reanalyse the data reported in this paper is available from the lead contact upon request.

EXPERIMENTAL MODEL AND STUDY PARTICIPANT DETAILS

Cell lines

HeLa, HEK and SH-SY5Y cell lines were maintained in Dulbecco's Modified Eagle Medium (DMEM) + Glutamax (Cat# 31966, Gibco) supplemented with 10% FBS (Cat# 10270, Gibco) and 10 IU/mL penicillin–streptomycin at 37°C and 5% CO_2.

Primary culture of mouse embryonic fibroblasts (MEF)

Spg4-KO mouse model was previously described.[29,105,106] Care and manipulation of mice were performed in accordance with national and European legislations on animal experimentation and approved by the institutional ethical committee. Primary cultures of fibroblasts were obtained from WT and Spg4-KO embryonic mice (E12-E13). Briefly, embryos were dissected to remove the head, the tail, and the red organs in Hanks Balanced Salt Solution (HBSS, Cat# H4641, Sigma-Aldrich) with 20 mM HEPES (Cat# H0887, Sigma-Aldrich) at 4°C.[107] Tails were used to genotype the embryos as previously.[29] Then the embryos were incubated with 0.25% trypsin/EDTA supplemented with 100 K/mL of DNaseI (Cat# 260913, Millipore) for 15 min at 37°C and then tissues were dissociated using a glass Pasteur pipette by pipetting up and down 10 times slowly every 5 min. Cells were plated at the density of 50000–100000 or 500000 on 12-mm- or 30-mm, respectively, on uncoated dishes or at $1*10^6$ in 25 cm^2 Flasks and maintained in DMEM (Cat# 31966, Gibco) supplemented with 10% FBS and 10 IU/mL penicillin–streptomycin at 37°C and 5% CO_2.

METHOD DETAILS

Constructs

Mouse cDNAs encoding full-length spastin (M1; Clone MGC: 54786, GenBank: BC046286.1), M1 carrying the missense mutation c.445C > Y (M1CY) and M1 lacking the AAA ATPase cassette (aa 1–338; M1Δ) tagged GFP were previously described.[16] M1 harboring the pathological point mutation c.496R > C (c.499R > C in human; M1RC)[56] was generated from M1-GFP by QuickChange II XL site-directed mutagenesis kit (Agilent Technologies, Santa Clara, CA, USA) according to the manufacturer's instructions. M1-Flag was obtained from the equivalent GFP constructs by cloning M1 cDNA into pCMV-FLAG-MAT-Tag-2 Expression Vector (Sigma-aldrich). The correct sequences of all constructs and the presence of the point mutation were verified by DNA sequencing. Mito-mCherry was a generous gift of Christelle Tesson.

cDNA transfection and siRNA knock-down

For immunofluorescence, PLA and video-microscopy experiments cell lines were plated at the density of 60000–100000 or 300000 respectively on 12-mm- and 30-mm-round uncoated glass coverslip. Cells at 60–70% of density were transfected or co-transfected with selected plasmids (0.5–2 μg) using Lipofectamine 2000 (Invitrogen) with a ratio of 1:2 respectively accordingly to manufacturer instructions. Cells were processed 16h after transfection.

For siRNA experiments in HeLa or HEK models, cells were plated at the density of 600000–800000 cells on 60 mm petri dishes and transfected with 25 nM 50-50 mix of two custom siRNA ON-TARGET plus (siRNA1: 5′-GAACUUCAACCUUCUAUAA-3′, siRNA2: 5′-UAUAAGUGCUGCAAGUUUA-3′, Dharmacon,[55]) to silence spastin using DharmaFECT1 transfection reagent accordingly to manufacturer instructions. An ON-TARGET plus non-targeting siRNAs (scramble, D-001810-10-05, Dharmacon) and mock transfection were used as controls. Cells were split after 24h on different support according to the experiment and processed 72h after the siRNA treatment. For rescue experiments, HeLa cells were transfected 24h after the split with GFP-tagged WT M1 spastin or mutated forms of the protein using Lipofectamine 2000 and finally processed the day after. For siRNA experiments in SH-SY5Y, cells were plated at the density of 1.5 million cells on 25 cm^2 flasks and transfected twice at 0h and 24h with 30 nM of the same custom siRNA ON-TARGET plus mix against spastin, or scramble, used for HeLa cells using 15 μL of Lipofectamine 2000. In some experiments cells were co-transfected with 1 μg of EGFP to identify transfected cells. Cells were split after 48h from the first transfection on different support according to the experiment and processed 72h after the siRNA treatment.

Drugs

Antimycin A, oligomycin, carbonyl cyanide-4 (trifluoromethoxy)phenylhydrazone (FCCP), histamine and ATP were from Sigma-Aldrich. Charbachol was from Merck Millipore. Dilutions of these drugs were prepared according to manufacturer instructions. When needed, drugs were kept as stock solution and working dilution were prepared freshly at each day of the experiment. Drugs were added to culture medium at the final concentrations and for the time indicated in the figures and figure legends.

Antibodies

Mouse monoclonal Ab (mAb) anti-spastin 6C6 (Cat# ab77144; WB 1:1000), rabbit polyclonal Ab (pAb) anti-β-tubulin (Cat# ab6046; WB 1:10000), mouse mAb anti-TOM20 (Cat# ab56783; WB 1:2500; IF 1:2000), rabbit pAb anti-IP3R (Cat# ab5804, PLA 1:600), mouse mAb anti-VDAC1 (Cat# ab14734, PLA 1:200) and rabbit pAb anti-VDAC1 (Cat# ab15895; WB 1:2 500; PLA 1:200) were from Abcam. Mouse mAb anti-IP3R3 (Cat# 610312, PLA 1:250; WB 1:1000) and mouse mAb anti-Cytochrome C (Cat# 556433; WB 1:5000) were from BD Biosciences. Mouse mAb anti-flag clone M2 (Cat# F1804; IF 1:500), mouse mAb anti-acetylated tubulin clone 6-11B-1 (Cat# MABT868, IF 1:1000; WB 1:100000) and mouse mAb anti-GAPDH 71.1 (Cat# G8795; WB 1:50000) and rabbit pAB anti-Sigma-1R (Cat# HPA018002; WB 1:1000) were

from Sigma-Aldrich. Rat mAb anti-tyrosinated tubulin clone YL1/2 (Cat# MAB1864, IF 1:750; WB 1:10000) was from Millipore. Rabbit pAb anti-calreticulin (Cat# PA3-900; IF 1:750) was from Thermoscientific. Rabbit pAb anti-TOM40 (Cat# 18409-1-AP; WB 1:4 000), rabbit pAb anti-TOM20 (Cat# 11802-1-AP; WB 1:2 000), rabbit pAb anti-MCU/CCDC109A (Cat# 26312-1; WB 1:1000), rabbit pAb anti-TOM70 (Cat# 14528-1-AP; WB 1:5000) and rabbit pAb anti-DRP1 (Cat# 12957-1-AP; WB 1:1000) were from Proteintech. Rabbit mAb anti-β-tubulin (Cat# 2128S; WB 1:5000) and rabbit pAb anti-Phospho-DRP1 (Ser616, Cat# 4494; WB 1:500) were from Cell Signaling. Secondary antibodies for immunofluorescence Alexa Fluor 488-, 594-, 647-conjugated goat anti-rabbit, anti-mouse or anti-rat were from Invitrogen (Carlasbad, CA, USA). Secondary antibody for immunoblot IRDye 800CW (1:15000) conjugated goat anti-rabbit was from LI-COR Bioscience and Alexa Fluor 680 (1:15000) conjugated goat anti-mouse was from Invitrogen.

Immunofluorescence, time-lapse imaging, and integrated fluorescence analysis

For immunofluorescence, cells were fixed with 4% PFA in PBS for 20 min at room temperature (RT) and then permeabilised with 0.1% Triton X-100 (Sigma-Aldrich) in 0.125% gelatine (Cat# G7765, Sigma Aldrich). Cells were then blocked in 0.25% gelatine and incubated ON at 4°C with selected primary antibodies diluted in 0.125% gelatine. Cells were then washed 3 times in 0.125% gelatine solution and incubated 1 h at RT with secondary antibodies diluted in 0.125% gelatine. Cells were finally washed 3 times with 0.125% gelatine and coverslips were mounted with DAPI-Fluoromount-G (Cat# 0100-20, Southern Biotech) before to be imaged.

For dual-color time-lapse video imaging of M1-spastin and mitochondria, HeLa cells were co-transfected with M1-GFP and mito-mCherry and analyzed 16–24 h after transfection using an inverted spectral confocal Leica SP8 scanning microscope (Leica Microsystems, Germany). Cells were imaged live every 10 s over a time of 5–10 min. Imaging was conducted in modified Krebs-Ringer-HEPES buffer (135 mM NaCl, 2.5 mM KCl, 1.2 mM $MgCl_2$, 2 mM $CaCl_2$, 20 mM HEPES, 11.1 mM glucose and pH 7.4). Temperature was controlled by warmed air (37°C). For live imaging analysis of ROS, $\Delta\Psi$m and mitochondrial mass, cells were incubated 30–45 min at 37°C 5% CO_2 in DMEM full medium with 2.5 mM MitoSOX Red (Cat# M36008, Invitrogen), 100–400 nM TMRM (Cat# I34361, Invitrogen) and 100 nM MitoTracker green (Cat# M7514, Invitrogen), respectively. In some experiments cells were co-incubated with two dyes. Cells were then imaged live in modified Krebs-Ringer-HEPES buffer using the same confocal microscope described above. MitoSOX Red, TMRM and mitotracker green were excited at 514 nm, 552 nm, and 488 nm, respectively.

Post-acquisition analysis of video and images were realized using semi-automatic custom-made scripts in Metamorph software (Roper Scientific, Evry, France). Briefly, to quantify M1-GFP movements on x-y axis in time-lapse video imaging experiments over 200 M1-GFP puncta were selected from forth different videos and tracked over time using Track Object tool. Objects moving less of 0.5 μm were considered static. For colocalization analysis individual channels were background subtracted, thresholded and the percentage of overlap of one channel into the other was quantified with Colocalization tool. For quantification of the average mitochondrial surface, images were background subtracted, thresholded and binarized. Surface area of individual mitochondria stained by TOM20 longer than 0.2 μm was measured automatically by Morphometric Analysis tool and the average was normalized to the surface of the cell. For analysis of TMRM, Mitosox Red and mitotracker green in living cells, images were background subtracted, then thresholded and the fluorescence intensity average of the relative dyes were analyzed in the ROIs of interested using the integrated morphometric analysis tool.

Proximity ligation assay (PLA)

PLA was realised with the Duolink *In Situ* Red kit according to the manufacturer instructions (Cat# DUO92101, Sigma Aldrich). Briefly, cells were first treated as for a classical immunofluorescence described above but after the incubation with the primary antibodies the cells were thoroughly washed 5 times with 0.125% gelatine and incubated 1h at 37°C with PLA probes PLUS and MINUS prepared as instructed by the manufacturer. Then cells were washed 3 times with wash buffer A and incubated 40 min at 37°C with the ligation mix. Cells were then washed again 3 times with wash buffer A then incubated 100 min at 37°C in the dark with the polymerisation mix. Cells were then washed 3 times with wash buffer B and coverslips were mounted with DAPI-Fluoromount-G. Images were captured with a spectral confocal Leica SP8 scanning microscope (Leica Microsystems, Germany). Quantification of surface of PLA puncta per cell surface was realized with custom semi-automatic script developed on Metamorph software. Briefly, PLA fluorescent spots were detected by auto-threshold detection of light objects tool, then a signal/background ameliorations was obtained by processing the images by a series of steps including binarization, elimination of isolated pixels, erosion, and dilatation. ROIs were then manually drawn around the border of all the cells in the field and the surface of PLA spots and the cell were automatically measured using the integrated morphometric analysis tool. In the case of siRNA-rescue experiments using spastin-GFP tagged constructs in HeLa cells and in PLA experiments in SH-SY5Y cells, the average fluorescence intensity of GFP was also measured for each cell to discriminate between transfected and untransfected cells and PLA surface was measured only in GFP positive cells.

Electronic microscopy

72h after siRNA treatment HeLa cells were fixed 1h at RT with 2% glutaraldehyde, 2% PFA in 0.1 M sodium cacodylate buffer pH 7.4 (EMS, Souffelweyersheim, France). Cells were then washed twice in 0.1 M sodium cacodylate buffer pH 7.4 and post-fixed with 1% osmium tetroxide in sodium cacodylate buffer (150 mM, pH 7.4, EMS, Souffelweyersheim, France). After washing in cacodylate buffer and water, samples were incubated in 2% aqueous uranyl acetate at 4°C ON. After rinsing twice in water, samples were dehydrated in increasing concentrations of ethanol (10% steps, beginning with 30% ethanol). Final dehydration took place in 100% ethanol (3 times, 15 min each). Samples were infiltrated 1h at RT once with 50% pure ethanol 50% Epon 812 (EMS, Souffelweyersheim, France) and then twice with 100% Epon 812. Gelatin capsules

filled with Epon 812 were placed upon the coverslips. Resin was cured for 48 h at 60°C in a dry oven. Ultrathin 70 nm thick sections were made with an UC7 ultramicrotome (Leica, Leica Microsystemes SAS, Nanterre, France) and collected on copper grids (200 mesh, EMS, Souffelweyersheim, France) that were then contrasted with Reynold's lead citrate (The use of lead citrate at high pH as an electron opaque stain in electron microscopy[108]). Observations were made with an HT700 120kV electron microscopy (Milexia, Saint Aubin 91190, France) operating at 100 kV and images (2048x2048 pixels) were acquired with an AMT41B camera. Mitochondria length or perimeter average were measured by manually tracing the outline of each individual mitochondria by using Metamorph software.

Immunoblot assays and subcellular fractionation

HeLa cells, HEK cells, SH-SY5Y cells or MEF were lysed in RIPA buffer (Pierce, Thermo Fisher, Waltham, MA) supplemented with protease inhibitors cocktail (Complete ULTRA Tablets, EDTA-Free, Roche) at 4°C for 20 min. After quantification by BCA (Pierce, Thermo Fisher, Waltham, MA), between 10 and 30 μg of proteins were separated by SDS-PAGE using 4–12% Bis-Tris NuPAGE 4–20% (Invitrogen, Carlasbad, CA, USA) in MOPS SDS running buffer and transferred to a nitrocellulose membrane (Amersham Protran, GE Healthcare Life Sciences) for 90 min at 300 mA. Membranes were then blocked in 50% Blocking buffer (LI-COR Biosciences, Lincoln, NE, USA) in PBS for 1h at RT and ON with specific primary antibodies diluted in 50% Blocking buffer in PBS. Membranes were washed 3 times in PBS supplemented with 0.1% Tween 20 (PBS-T) and then incubated with secondary antibodies in PBS-T. Membranes were then washed 3 times in PBS-T and detection was carried out by Odyssey infrared imaging system (LI-COR Biosciences, Lincoln, NE, USA). The fluorescence intensity of each band was quantified by densitometry analysis using the ImageJ software (Rasband, W.S., ImageJ, U. S. National Institutes of Health, Bethesda, MD, USA, http://imagej.nih.gov/ij/). The measurements were normalized to GAPDH intensity of each sample.

Fractionation was performed as described previously.[38,109] Briefly, HeLa cells (10^9) were harvested, centrifuged at 500 g for 5 min with PBS and resuspended in homogenization buffer (225 mM mannitol, 75 mM sucrose, 30 mM Tris-HCl pH 7.4, 0.1 mM EGTA and PMSF). Liver and brain tissue isolated from WT C57Bl/6 mice were cut into small pieces and resuspended in homogenization buffer for tissues (225 mM mannitol, 75 mM sucrose, 0.5% BSA, 0.5 mM EGTA and 30 mM Tris-HCl pH 7.4). The homogenate (from cells or tissues, gently disrupted by Dounce homogenization) was centrifuged twice at 600g for 5 min and then the supernatant was centrifuged at 9000g for 10 min to pellet crude mitochondria. The resultant supernatant was centrifuged at 20000 g for 30 min at 4°C; the pellet consists of lisosomal fraction also containing plasma-membrane contamination. Further centrifugation of the obtained supernatant (100000 g for 1h) results in the isolation of cytosolic fraction (supernatant) and ER (pellet). The crude mitochondrial fraction was subjected to Percoll gradient centrifugation at 95000*g* for 30 min. Pure mitochondrial fraction was resuspended in MRB buffer (mitochondria resuspending buffer): 250 mM mannitol, 5 mM HEPES (pH 7.4) and 0.5 mM EGTA); MAM fraction was centrifuged at 100000 g for 90 min at 4°C and then collected. IP3R3, SigmaR1, β-tubulin, VDAC1 and Cytochrome *c* were used as ER, MAMs (MERCs), cytosol, and pure mitochondria markers, respectively.

FACS and mitochondrial probes

HeLa cells, HEK cells or mouse fibroblasts grown on 6 well plates or 60 mm petri dishes were collected and counted with Countess3 cell counter (Invitrogen). Equal number of cells from the different experimental conditions were then incubated with 100 nM Mitotracker green or 1 mM JC-1 (Cat# T3168, Invitrogen) or 2.5 mM MitoSOX Red for 30 min at 37°C 5% CO_2 in DMEM full medium. Cells were then washed twice with PBS and finally resuspended in 500 μL of modified Krebs-Ringer-HEPES buffer (135 mM NaCl, 2.5 mM KCl, 1.2 mM $MgCl_2$, 2 mM $CaCl_2$, 20 mM HEPES, 11.1 mM glucose and pH 7.4). Data were acquired on a Cytoflex LX flow cytometer (Beckman Coulter, USA) equipped with six active lasers and 21 channels for fluorescence detection and supplied with computer workstation with CytExpert Acquisition software cytEXPERT 2.4 (Beckman Coulter, USA). Cells were first selected based on their morphology parameters, their size and granulosity (FCS vs. SSC) at 488 nm and then we selected the singulet (FCS-A vs. FCS-H). MitoTracker green, JC1 and MitoSOX were excited at 488 nm. The emission filters were 525-40 nm for JC1-green channel and MitoTracker green, 610-20 nm for JC1-red channel and MitoSOX.

Ca^{2+} measurement

HeLa cells, SH-SY5Y cells or mouse fibroblasts grown on 13-mm-round glass coverslips at 50% confluence were transfected with the appropriate mitochondrial (mt), cytosolic (cyt), or endoplasmic reticulum (er) targeted aequorin (Aeq) chimeras as previously described.[71] All aequorin measurements were performed in Krebs-Ringer buffer (KRB; 135 mM NaCl, 5 mM KCl, 1 mM $MgSO_4$, 0.4 mM KH_2PO4, 5.5 mM glucose, 20 mM HEPES, pH 7.4) supplemented with 1 mM $CaCl_2$. Briefly, for the experiments with mtAeq (wt or mut) and cytAeq, cells were incubated with 3 μM coelenterazine for 2h in 0.1% FBS medium, and then transferred to the perfusion chamber. To reconstitute erAeq with high efficiency, the luminal Ca^{2+} concentration ($[Ca^{2+}]$) of the ER ($[Ca^{2+}]_{er}$) first had to be reduced. This was achieved by incubating cells for 1 h at 4°C in KRB supplemented with 5 μM coelenterazine, 5 μM Ca^{2+} ionophore ionomycin, and 600 μM EGTA. After this incubation, cells were extensively washed with KRB supplemented with 2% bovine serum albumin and then transferred to the perfusion chamber. Agonists, 100 μM histamine or 500 μM carbachol (Cch), 100 μM ATP were added to the medium, as specified in the Figure 5. The experiments were terminated by lysing the cells with 100 μM digitonin in a hypotonic Ca^{2+}-rich solution (10 mM $CaCl_2$ in H_2O), thus discharging the remaining aequorin pool. The light signal was collected and calibrated into $[Ca^{2+}]$ values by an algorithm based on the Ca^{2+} response curve of aequorin at physiological conditions of pH, $[Mg^{2+}]$, and ionic strength.

Measure of oxygen consumption rate (OCR)

Seahorse XFe96 Extracellular Flux Analyzer (Seahorse Biosciences, Agilent Technology, USA) was used to measure mitochondrial oxygen consumption rate (OCR). To this end, MEF obtained from 2 WT to 2 Spg4-KO mouse embryos (20 x 10^3 cells per well) were grown in DMEM supplemented with 10% FBS in a 96-well plate at 37°C and 5% CO_2 for overnight. On the day of the assay, the culture medium was changed to XFi Assay Medium supplemented with 1 mM pyruvate, 1X Glutamax and 5.5 mM glucose. The OCR was measured at baseline and after subsequent stepwise injection of the mitochondrial respiratory chain inhibitors, 10 mg/mL oligomycin, 5 μM FCCP and 10 μM Antimycin A. The OCR readings were normalized to cell number measured by DNA quantification/well with Hoechst labeling and fluorescence measurement. A range was used to calculate the number of cells according to the amount of fluorescence detected. Multiple parameters of mitochondrial respiration were calculated based on the response of the cells to the respiratory chain inhibitors: (a) basal respiration, difference between basal OCR and non-mitochondrial respiration rate; (b) ATP production, difference in OCR before and after oligomycin treatment; (c) maximal respiration, difference between OCR measurement after FCCP treatment and oligomycin treatment; and (d) spare respiratory capacity, difference between maximal respiration and basal respiration. The mean values are based on 20 replicates/point. OCR was recorded and calculated by the Seahorse XFe96 Software, Wave (Seahorse Biosciences). The OCR data were expressed as pmol/min/20000 cells.

Analysis of total ATP levels

ATP total levels was determined by luciferin/luciferase assay using the ATP Determination Kit (Cat# A22066, Invitrogen) as described previously.[110,111] Briefly, proteins were extracted from 4 different WT and 4 different Spg4-KO MEF lines using passive lysis buffer (Cat# E194A, Promega) for 15 min at RT. Between 5 and 10 μg of supernatants were then analyzed with the ATP determination kit according to manufactured instructions using a 2300 EnSpire luminometer Multimode Plate Reader (PerkinElmer).

QUANTIFICATION AND STATISTICAL ANALYSIS

All data are presented as the mean ± SEM. Data were analyzed using GraphPad Prism 9. The statistical tests used for each experiment are indicated in the respective figure legend. Sample sizes analyzed are indicated in the figure for each experiment. For two-group comparisons, statistical significance was determined by two-tailed Student's t tests. Multi-groups were analyzed using one-way ANOVA or two-way ANOVA. Statistical significance was defined in the figure panels as follows: *$p < 0.05$; **$p < 0.01$; ***$p < 0.005$; ****$p < 0.001$; ns, not significant.